*Manuscript
Click here to view linked References

Modelling heat and mass transfers in DCMD using compressible membranes

Jianhua Zhang[a], Stephen Gray[a], Jun-De Li[a, b*]

[a]*Institute of Sustainability and Innovation, Victoria University, PO Box 14428, Melbourne, Victoria 8001, Australia*

[b]*School of Engineering and Science, Victoria University, PO Box 14428, Melbourne, Victoria 8001, Australia*

**Corresponding author, Tel.: +61-3-9919 4105, E-mail: jun-de.li@vu.edu.au*

Abstract

A model for predicting the flux and evaporation ratio in Direct Contact Membrane Distillation (DCMD) using a compressible membrane is presented. Polytetrafluoroethylene (PTFE) membranes, one of the most common types of membranes employed in MD, are characterised with high porosity (~90%) and high hydrophobicity, and therefore have high water vapour permeability and high wetting resistance. However, the PTFE membrane is compressible due to its structure. Compression of the membrane will cause a change of its physical structure, such as porosity, thickness, and pore size. As a result, the thermal conductivity and vapour permeability of the membrane will be altered, causing a change in flux and energy efficiency. Such effects need to be accounted for when scaling up from laboratory data to full scale design, because there may be significant differences in the applied pressure. Therefore, in this paper, the influence of pressure on the flux of the compressible PTFE membrane was modelled. This paper also provides a mathematical method to correlate the applied pressures with physical structure changes based on the assumption of constant tortuosity. The modelling results were compared with experimental results over a range of variable process parameters, i.e., temperatures, velocities, membrane lengths, and pressure applied to the membrane. The errors between the model predictions and experimental results were less than 10% within the operating range used in this investigation.

Keywords:

Direct contact membrane distillation, desalination, flux modelling, compressible membrane

1. Introduction

Membrane distillation (MD) is a membrane-based separation process, for which the driving force of separation is a vapour pressure difference across the membrane. The vapour pressure difference arises because of either a temperature difference across the membrane or a reduced vapour pressure on one side of the membrane. In comparison with other thermal desalination processes, the path length of vapour transport in MD is much smaller than that for multi-stage flash, multi-effect distillation and vapour compression, and is approximately the same as the membrane thickness (~100 μm). MD can also be used to treat high concentration or supersaturated solutions, because its driving force is not as sensitive to salt concentration as is the case for Reverse Osmosis (RO) [1, 2]. The capability of utilising low grade heat makes it possible to combine with solar heating, or sources of waste heat from power stations, chemical plants and other industries, to produce high purity water.

The characteristics of MD [1] membranes are: microporous, unwetted by process liquid, and do not altering the vapour equilibrium of different components in the process liquids. Additionally the MD process requires that no capillary condensation occurs inside the membrane pores, only the gas phase is able to pass through the pores, and the driving force for mass transfer is the partial pressure gradient across the membrane. In comparison with other desalination methods, MD has advantages such as: a nearly complete rejection of non-volatile components, a low operating pressure that is not related to feed concentration as is the case for reverse osmosis (RO), a simple structure and operation, a small vapour space, and low operating temperatures (40-80°C) [1]. These characteristics make it a promising technique for desalination where low grade heat is available, such as in industrial sites. Furthermore, high salinity wastewater, such as the concentrate from RO processes, is difficult to treat by RO because of the high osmotic pressure and the presence of scaling compounds. MD could be used after RO to recover additional water from the concentrate streams and thus reduce the volume of brine for disposal.

In our MD pilot plant using compressible flat sheet PTFE membrane, a dramatic flux decrease was found in comparison with laboratory scale results under similar operating conditions. This reduction of flux was greater than the predicted flux reduction if only changes in length were considered. It was expected that the pressure drop would be much higher in the flow channel of the pilot/industry scale module than the laboratory scale module, due to longer flow channels. It was also found in our research that the performance of the compressible membrane was related to the pressure applied on its surface [2] in MD. Former MD modelling [3] has mainly focused on membranes with constant properties that are unaffected by pressure. However, as compressible membranes are subjected to external pressure, the physical properties, such as thickness, pore size and porosity are altered, so as to cause the changes of its thermal conductivity and permeability. In this paper, the pore size, porosity, thickness and thermal conductivity of the membrane are not considered as constants but are varied with applied pressure. Although the relationship between the flux and membrane length was included in the modelling for hollow fibre DCMD [4-6], it was rarely considered for the flat sheet modules with spacer filled channels.

1.1 Heat transfer

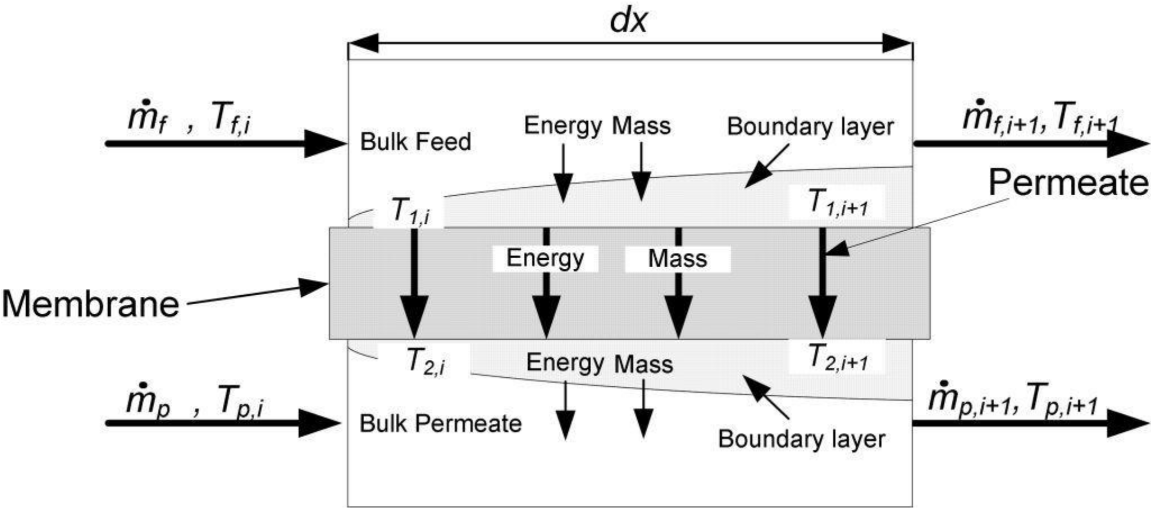

Fig.1 Heat and mass transfer through the membrane

In DCMD, the driving force for mass transfer is the vapour pressure difference that arises from the temperature difference between the liquids on both sides of the membrane. Thus, DCMD performance relies on the complex relationships between simultaneous heat and mass transfers, which are in the same direction from the feed side to the permeate side. In Fig. 1, dx is the length of the small element which is located at a distance x from the inlet of the hot feed, and the subscript i is the i^{th} element from $x = 0$. Based on Fig. 1, for the feed side:

$$Q_{f,transfer} = \alpha_f (T_f - T_1) W dx \quad (1)$$

For permeate side:

$$Q_{p,transfer} = \alpha_p (T_2 - T_p) W dx \quad (2)$$

where $Q_{f,transfer}$ is the absolute overall heat transfer and T_1 and T_2 are the interface temperatures at the interface of the membrane with the feed and permeate streams.

The heat transfer through the membrane is:

$$Q_{f,transfer} = \left(\frac{\lambda}{b}(T_1 - T_2) + JH_{g,T1}\right)Wdx, \text{ or}$$

$$Q_{p,transfer} = \left(\frac{\lambda}{b}(T_1 - T_2) + JH_{g,T2}\right)Wdx \qquad (3)$$

where H_g is the enthalpy of the vapour, W is the width of the membrane, and J is the flux

Supposing the difference between T_1 and T_2 is as great as 40°C, the enthalpy difference of the vapour (60 °C and 20°C) is about 71 kJ/kg [7], which is only 3% of the enthalpy of vapour at 20°C. If the average vapour enthalpy in the pore is used, the difference will be only about 1% of the enthalpy of vapour at 20°C. If a temperature polarisation coefficient (TPC) of 0.5 (in our work the highest TPC < 0.35) is applied, the temperature difference of T_1 and T_2 should be less than 20°C, and the enthalpy difference between the average enthalpy and enthalpy of T_1 and T_2 will be less than 0.5%. Therefore, it can be assumed that:

$$\bar{H}_{g,pore} \approx H_{g,T1} \approx H_{g,T2} \qquad (4)$$

It can be deduced that [8, 9]:

$$Q_{f,transfer} \approx \left(\frac{\lambda}{b}(T_1 - T_2) + J\bar{H}_g\right)Wdx \approx Q_{p,transfer} \qquad (5)$$

where $\bar{H}_g$ is the enthalpy of the vapour in the pore, λ is the thermal conductivity of the membrane, and b is the membrane thickness.

In Eq. (5), $\lambda(T_1\text{-}T_2)/b$ is the sensible heat transfer across the membrane and $J\bar{H}_g$ is heat transfer accompanying the mass transfer. Therefore, the evaporation ratio (expressed in percentage) used for evaporation (E) can be defined as [10]:

$$E = \frac{J\bar{H}_g}{Q_{f,transfer}} \times 100\% \qquad (6)$$

The heat transfers across the feed, membrane and permeate should balance, and thus:

$$\alpha_f(T_f - T_1)Wdx = \left(\frac{\lambda}{b}(T_1 - T_2) + J\bar{H}_g\right)Wdx = \alpha_p(T_2 - T_p)Wdx \qquad (7)$$

The thermal conductivity in this paper was initially measured experimentally using a similar method to Garcia-Payo and Izquierdo-Gil [11]. This method required placing the membrane between two copper plates and measuring the heat flow between the copper plates. However, it was found the results were not valid, because it was hard to make perfect contact between the compressible membrane and the copper discs without compressing the membrane. Therefore, it is difficult to judge if the measured thermal conductivity was overestimated (if the membrane was compressed) or underestimated (if contact was not good).

For the calculation of thermal conductivity of porous membranes, studies [11, 12] have determined mathematic models to fit experimental results. In these papers, a method to ensure good contact between the membrane and copper discs was mentioned, but there was no discussion of whether this contact caused deformation of the membrane, especially for the PTFE membranes studied. Therefore, these models may be not applicable for the PTFE compressible membranes used in this study. Furthermore, the tortuosity factor of the employed PTFE membrane was about 1.1 [2]. This indicates that the pore channels were approximately straight and perpendicular to the membrane surface, so it can be speculated that the pores and the solid walls between the pores were aligned almost parallel. Therefore, a conservative and popular parallel model [8, 9, 13] in MD modelling was used to calculate thermal conductivity of the active layer:

$$\lambda_{active} = \lambda_{air}\varepsilon + \lambda_{solid}(1 - \varepsilon) \qquad (8)$$

where λ_{active}, λ_{air} and λ_{solid} are thermal conductivities of the active layer, air and the solid material , respectively, and ε is the membrane porosity.

The TPC [14] for DCMD is normally used to access the process efficiency of DCMD and is defined as:

$$TPC = \frac{T_1 - T_2}{T_f - T_p} \tag{9}$$

1.2 Mass transfer in DCMD

The hydrophobic MD membrane is a porous medium. The mass transfer through such medium can be interpreted by three kinds of basic mechanisms: Knudsen diffusion, molecular diffusion and Poiseuille flow [15]. The Knudsen number (*Kn*)

$$Kn = l/d \tag{10}$$

is used to judge the dominating mechanism of the mass transfer in the pores. Here, *l* is the mean free path of the transferred gas molecules and *d* is the mean pore diameter of the membrane.

Table 1 shows the dominating mass transfer mechanism based on *Kn* in a gas mixture with a uniform pressure throughout the system [16].

Table 1
Mass transfer mechanism in membrane pore

Kn<0.01	0.01<*Kn*<1	*Kn*>1
molecular diffusion	Knudsen-molecular diffusion transition mechanism	Knudsen mechanism

As the pore size of the MD membranes is in general in the range of 0.2-1.0 μm [17] and the mean free path of the water vapour is 0.11 μm at a feed temperature of 60°C [18], *Kn* calculated from Eq. (10) is in the range of 0.55-0.11. Therefore, Knudsen-molecular transition diffusion is the dominating mass transfer mechanism within the pores [18, 19]. Since the mean pore size of the membrane was measured using a gas permeation technique, but used as the mean pore size for modelling gas diffusion across the membrane, the pore size distribution has the potential to affect the mass transfer modelling results. However, Woods et. al [20] have shown that the effect of pore size distribution is small compared to the uncertainties in modelling and experimental reproducibility for DCMD. Therefore the effect of pore size distribution was ignored in this model.

With this assumption, the overall mass flux across the membrane can be expressed as:

$$\frac{1}{J} = \frac{1}{J_k} + \frac{1}{J_m} = \frac{1}{\frac{4}{3} d \frac{\varepsilon}{b\tau} \sqrt{\frac{1}{2\pi RMT}} \Delta P} + \frac{1}{\left(\frac{1}{1-x_A} \cdot \frac{\varepsilon}{b\tau} \cdot \frac{D_{AB}}{RT} \right) \Delta P} \tag{11}$$

where J_m and J_k are the vapour flux through the membrane arising from molecular and Knudsen diffusion, τ is the pore tortuosity factor, R is the universal gas constant, M is the molecular mass of the vapour, D_{AB} is the diffusivity of water (A) to air (B), x_A is the mole fraction of water in the pore and P_{T1} and P_{T2} are the vapour pressures at temperature T_1 and T_2, which can be calculated by the Antoine equation [21].

2. Theory

2.1 Variation of membrane properties with pressure

Mass transfer of compressed membranes

In Eq. (11), the diffusivity (D_{AB}) of water vapour (A) relative to air (B) can be modelled in membrane distillation as [19, 22]:

$$D_{AB} = \frac{1.895 \times 10^{-5} T^{2.072}}{P} \tag{12}$$

In this study, as the absolute pressure (100- 160 kPa) in the pores is low, the water vapour and air in the pores can be assumed an ideal gas mixture. Therefore, the mole fraction of the water vapour x_A can be calculated as:

$$x_A = \frac{P_A}{P} \tag{13}$$

So the total vapour flux across the membrane shown in Eq. (11) can be derived as:

$$J = 7.81 \times \frac{\varepsilon d}{b\tau} \frac{MT^{1.072}}{5.685\sqrt{2\pi RMT} + 4dR(P-P_A)} (P_{T1} - P_{T2}) \tag{14}$$

As the membrane is compressed, it has been shown [8] that the thickness of the active layer is reduced. As a result, the pore size, porosity and tortuosity are expected to change. As the active membrane layer considered in this work was a uniform membrane (ie. non-asymmetric) with a coarse, porous scrim support, the porosity can be calculated as:

$$\varepsilon = \frac{V_{void}}{V_a} = \frac{N_0 \frac{\pi d^2}{4} b\tau^{0.5}}{b} = N_0 \frac{\pi d^2 \tau^{0.5}}{4} \tag{15}$$

where N_0 is the nominal number of pores per square meter in the active layer, and V_{void}, and V_a are the void volume and total volume of the active layer, respectively. In Eq. (15), we have assumed that the pores are cylindrical. Because porosity and pore size can be measured by the methods provided in [2], N_0 can be estimated by:

$$N_0 = \frac{4\varepsilon_0}{\pi d_0^2 \tau_0^{0.5}} \tag{16}$$

Here subscript *0* is for membrane under no compression. Under the assumption that N_0 does not change with pressure, using the changes in membrane thickness and porosity with pressure determined experimentally, the pore size under different pressures can be calculated by:

$$d_p = \sqrt{\frac{4\varepsilon_p}{N_0 \pi \tau_p^{0.5}}} \tag{17}$$

where ε_p, τ_p and d_p are the porosity, tortuosity factor and pore diameter of the membrane at pressure P. In Eq. (17), the change of tortuosity factor (τ_p) with pressure is unknown for the employed PTFE membrane, but was assumed not to change greatly for the pressure range considered , i.e. it is assumed $\tau_p = \tau_0$. This assumption was based on a calculated tortuosity factor around 1.1 [2], i.e. the pores were almost vertically aligned, and pressure applied normally will not distort the pores in the direction normal to the membrane greatly. Therefore, the compression of the membrane does not affect the ratio of pore length to membrane thickness (tortuosity) greatly, as the pore length is almost equal to the membrane thickness.

The total flux of a membrane under pressure can thus be expressed as:

$$J = 7.81 \times \frac{\varepsilon \sqrt{\frac{4\varepsilon_p}{N_0 \pi \tau_0^{0.5}}}}{b\tau_0} \frac{MT^{1.072}}{5.685\sqrt{2\pi RMT} + 4\sqrt{\frac{4\varepsilon_p}{N_0 \pi \tau_0^{0.5}}} R(P-P_A)} (P_{T1} - P_{T2}) \tag{18}$$

Eq. (18) can also be simplified to:

$$J_p = C_{membrane,p} (P_{T1} - P_{T2}) \tag{19}$$

where $C_{membrane,p}$ is the mass transfer coefficient of the membrane under pressure.

Thermal conductivity of the compressed membrane

As shown in Eq. (8), the thermal conductivity of the membrane is related to the porosity. For a compressed membrane, the porosity decreases so the thermal conductivity of the membrane increases. Since the porosity change with pressure is experimentally measurable, the variation of thermal conductivity of the active layer with pressure can be estimated via Eq. (8) [2]. The thermal conductivity of the whole membrane was calculated by adding the thermal conductivities of the scrim layer and the active layer in series.

2.2 Theoretical analyses of the heat transfer and mass transfer

When developing a model for heat and mass transfer across the membranes, the following assumptions were made:

- no heat loss through the module wall (< 1% estimated heat loss of the feed),
- the heat of vaporisation and condensation does not change with concentration, because low concentration feed (1 wt%) was used, and no obvious difference between deionised water and this feed was found in the previous experiments,
- the tortuosity does not change with pressure,
- in balancing the heat transfer, variations in latent heat at different interface temperatures is ignored, and
- there is no temperature gradient across the width of the membrane (i.e. perpendicular to the flow direction.

To analyse the heat transfer between the hot feed and the cold permeate, a small element was considered as shown in the schematic diagram in Fig. 1. Based on Fig. 1, the energy balance equations for feed and permeate temperatures distributed along the membrane can be written as:

$$\dot{m}_{f,i}h_{f,i} = \dot{m}_{f,i+1}h_{f,i+1} + Q_{transfer,i}, \text{ and}$$
$$\dot{m}_{p,i}h_{p,i} + Q_{transfer,i} = \dot{m}_{f,i+1}h_{p,i+1} \quad (20)$$

where $\dot{m}_f$ and $\dot{m}_p$ are the mass flow rates of the feed and permeate, and $h_{f,i}$ and $h_{p,i}$ are the enthalpies of the feed and permeate.

Due to the mass transfer across the membrane, the mass flow rates of the feed and permeate are related as:

$$\dot{m}_{f,i} = \dot{m}_{f,i+1} + J_iWdx, \text{ and}$$
$$\dot{\mathrm{m}}_{\mathrm{p,i}} + \mathrm{J_iWdx} = \dot{\mathrm{m}}_{\mathrm{p,i+1}} \quad (21)$$

By using the $Q_{f,transfer}$ and $Q_{p,transfer}$ from Eqs. (1) and (2), the temperature of the feed and permeate at *i+1* can be calculated as:

$$T_{f,i+1} = \frac{\dot{m}_{f,i}C_{p,f,i}T_{f,i} - \alpha_f(T_{f,i} - T_{1,i})Wdx}{C_{p,f,i+1}\dot{m}_{f,i+1}}, \text{ and}$$
$$T_{p,i+1} = \frac{\dot{m}_{f,i}C_{p,p,i}T_{p,i} + \alpha_p(T_{p,i} - T_{1,i})Wdx}{C_{p,p,i+1}\dot{m}_{p,i+1}} \quad (22)$$

where $C_{p,f}$ and $C_{p,p}$ are the specific heats of the feed and permeate.

3. Experiment and simulation

3.1 Membrane characterisation

Membrane materials were provided by Changqi Co. Ltd and consisted of a polytetrafluoroethylene (PTFE) active layer and a polypropylene (PP) scrim support layer. The nominal pore size was 0.5 µm.

SEM characterisation

The active layer, support layer and the cross section (thickness) of the membrane were observed by a Philips XL30 FEG Scanning Electron Microscope (SEM). The membrane was fractured following immersion in liquid nitrogen to form an intact cross section [10] before it was scanned.

Air permeability measurement

The pore size of the membrane and $d_0\varepsilon_0/b_0\tau_0$ were estimated by the gas permeability method [19] using compressed nitrogen and by varying the pressure in the range of 5-80 kPa. The pressure difference across the membrane was set at 1.00±0.01 kPa. A digital manometer (645, TPI) was used to measure the pressure and the pressure difference. A stopwatch was used to record the time. Five samples from the different parts of a membrane were tested, and the average value was used in subsequent analysis. A schematic drawing of the apparatus is shown in Fig. 2.

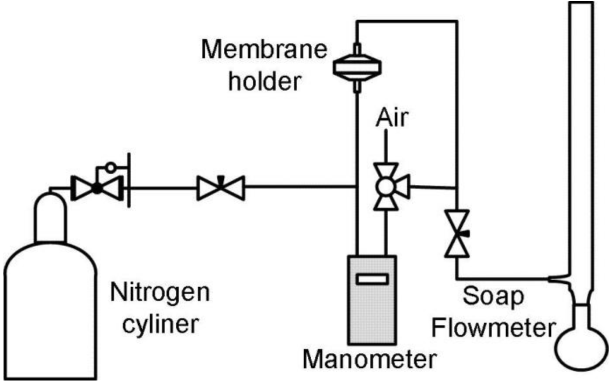

Fig. 2 Air permeability testing instrument

Measurement for porosity, thickness and compressibility

The porosity and thickness of the membrane under different pressures were measured with the method provided in [2]. When the thickness of the membrane as a function of pressure was measured at elevated temperatures, the pressurised chamber was placed in a water bath and the temperature stabilised over several hours before measurements were taken to guarantee no air bubbles occurs, and a blank test was also done under the same operation conditions.

3.2 Experimental process

Experiments under different conditions were performed to verify the model. A schematic diagram of the DCMD process is shown in Fig. 3.

For the experiments performed under low pressure (0 - 3 kPa), the pressure control valves were fully open. The velocities of the feed and permeate streams were varied from 0.055 to 0.151 m/s (300-800 mL/min), and the feed and permeate streams were maintained at the same velocity in all experiments using two peristaltic pumps. The flowrate was calibrated using a volumetric cylinder and the accuracy was ±10 mL/min. Two digitally controlled water baths (refrigerated and heated) were used to control the inlet temperatures of permeate at 20±2°C and feed in the range of 30-70±2°C. The brine feed was prepared by dissolving 50 g NaCl in 5 L water (10 g.L^{-1}). Four temperature sensors were used to measure the temperatures of the hot brine and cold permeate streams at their inlets and outlets. A conductivity meter in the product reservoir was used to monitor changes in conductivity, which were used to calculate salt rejection and to monitor for leaks. Flux was determined by measuring the weight of the product reservoir over time and was calculated based on the membrane area. The membrane length was varied in the range of 50-130 mm. A larger module with an active membrane size of 200×733 mm was also used to verify the model.

The experiments with pressure applied on the membranes were described in Zhang et. al [2]. Four series of experiments were performed including two series in which the pressure was varied at the velocities of 0.0945 and 0.114 m/s (520 and 620 mL/min) at hot and cold inlet temperatures of 60 and 20°C, respectively. For the other two series the pressure was varied for hot stream inlet temperatures of 50 and 70±2°C at velocities of 0.0945 m/s. All experiments were conducted with identical pressures in the feed and permeate streams and the pressures varied from 3 to 45±3 kPa.

All flux results were measured over a period of 2.5 to 4 hours and variation in flux (calculated every half or one hour) over this time was ±5%. Most experiments were repeated under the same conditions, variations of flux were found in the range of ±5% when different portions of a membrane were employed. Except for data presented in the chart showing the influence of membrane length on flux, all the data presented in each figure were from a piece of new membrane. Before the membranes were used, they were conditioned for 3 h at feed and permeate inlet temperatures of 60 and 20°C and velocity of 0.0945 m/s with pressure control valves fully opened. In the conditioning period (no membrane compression), only the membranes with initial flux falling into the range of ±5% of the average flux were selected for further experiments.

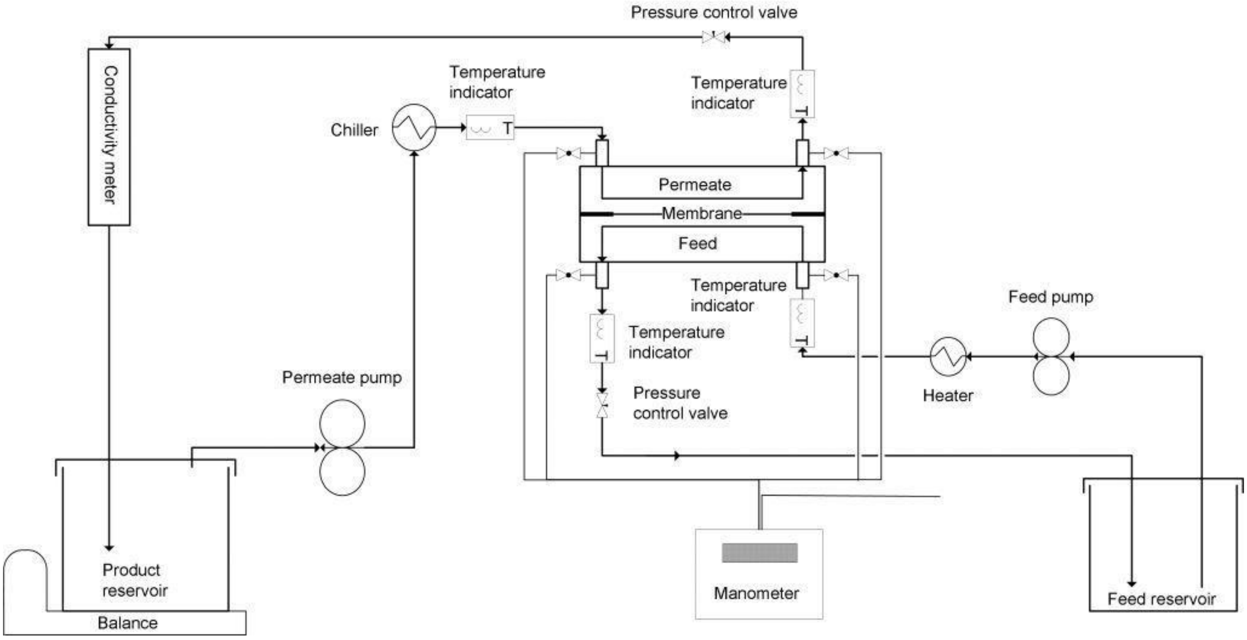
Pressure control valve
Conductivity meter
Temperature indicator
Temperature indicator
Chiller
Permeate
Membrane
Feed
Temperature indicator
Temperature indicator
Feed pump
Permeate pump
Pressure control valve
Heater
Product reservoir
Balance
Manometer
Feed reservoir

Fig. 3 Schematic diagrams of the employed DCMD process

3.3 Modelling heat and mass transfer for spacer filled channel

The spacer used was 0.8 mm thick and composed of filaments (ϕ = 0.4 mm), as shown in Fig. 4. The spacer was used to support the membrane and it also acted as a turbulence promoter. The spacer porosity was measured experimentally and calculated using [10],

$$\varepsilon_{spacer} = \frac{V_{filament}}{V_{spacer}} \qquad (23)$$

where ε_{spacer} is the porosity of the spacer, $V_{filament}$ is the volume of spacer filament and V_{spacer} is the total spacer volume.

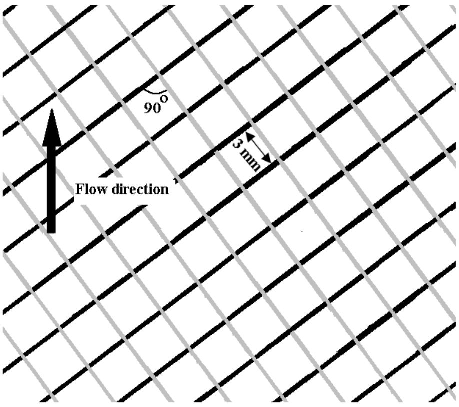
90°
3 mm
Flow direction

Fig. 4 Spacer structure and stream direction

Because temperature varies as the hot and cold streams flow along the DCMD module, water properties (viscosity, saturated vapour pressure and latent heat) need to be calculated at each point along the membrane length to account for the change in temperature. Therefore, a Nusselt number (*Nu*) that varied with the local temperature was used for the calculation of convective heat transfer coefficient, rather than an average Nusselt number as used in [22]. From the Nusselt number, the local convective heat transfer coefficients (α_f, α_p) can be calculated [23].

For the spacer filled channel, although the *Reynolds number* was less than 300, the model predictions fit the experimental data better when an approximate solution recommended by [24, 25] of local *Nu* on a flat surface of fully developed turbulent flow was used in the modelling:

$$Nu = 0.0292 Re^{0.8} Pr^{0.33} \tag{24}$$

For the spacer filled channel, the Nusselt number needed to be calibrated by a spacer factor K_s [22, 26],

$$Nu_s = K_s Nu \tag{25}$$

where K_s is the spacer factor:

$$K_s = a \left(\frac{\phi}{h_s}\right)^c \varepsilon_{spacer}^d \left(\sin\frac{\theta}{2}\right)^e \tag{26}$$

where θ is the angle between filaments as shown in Fig. 4 and h_s is the thickness of the spacer. In this work, a = 1.9, c = 0.039, d = 0.75, and e = 0.086 are coefficients mainly from the work of Phattaranawik, J. al et. [26], except for a which is 1.15 times the value the given in [26]. The coefficient a was adjusted based on the experiment with stream velocities at 0.114 m/s and membrane length of 0.13 m, and inlet temperatures of feed and permeate of 60˚C and 20°C, and it was verified with different stream velocities, temperatures, membrane lengths and pressures.

3.4 Numerical solution

The DCMD flow channel in the module was divided into small elements *dx*, and solved numerically. This numerical solution was implemented using the MATLAB.

For counter-current flows, $x = 0$ was taken at the inlet of the hot feed and the mass flowrate on the cold permeate side was taken as a negative value. An iteration procedure was used to solve the system of equations [27].

Based on Eq. (7), the membrane interface temperatures $T_{1,j}$ and $T_{2,j}$ were calculated by first determining the overall heat transfer using [19]:

$$Q_{f,transfer,i} \approx Q_{p,transfer,i} = \frac{T_{f,i} - T_{p,i} + J_i H_{g,i}\left(\frac{b}{\lambda}\right)}{\frac{1}{\alpha_{f,ij}} + \frac{1}{\alpha_{p,i}} + \frac{b}{\lambda}} W dx \tag{27}$$

For given flowrates and geometry, the heat and mass transfer coefficients at $x = x_j$ were calculated using Eq. (9) and the bulk temperatures $T_{f,j+1}$ and $T_{p,j+1}$ were obtained. From Eqs. (1) and (2), these can be approximated as:

$$T_{1,i+1} = T_{f,i} - \frac{Q_{f,transfer,i}}{\alpha_{f,i}} \tag{28}$$

$$T_{2,i+1} = \frac{Q_{p,transfer,i}}{\alpha_{p,i}} + T_{p,i} \tag{29}$$

For the $(i+1)^{th}$ element, the mass flow rate on the feed side is reduced and that on the permeate sides is increased due to the vaporisation, so the feed and permeate bulk temperatures were calculated using Eq. (22).

4. Results and discussion

4.1 Analytical results and discussion

Table 2 lists the measured and calculated membrane properties. The mean pore size measured by the gas permeation was similar to the nominal pore size provided by the manufacturer (0.5 μm).

Table 2
Properties of PTFE membrane

d_0 (μm)	ε_0 (%)	b_0 (μm)	$d_0\varepsilon_0/b_0\tau_0$ ($\times 10^{-3}$)	τ_0	λ_0/b_0 ($W \cdot K^{-1} \cdot m^{-2}$)	N_0 ($\times 10^{12}$ m^{-2})
0.5±0.08	91±0.5	46±1	8.7±0.7	1.08±0.03	980±40	4.0±0.2

The deformation of the compressible PTFE membrane under different pressures was reported in [2].

The structures of the active layer are shown in Fig. 5. The images show that the PTFE active layer has a web like structure, so that it is very difficult to determine the pore size directly by visualisation, as there were no obvious pores. The stretching-formed filament structure provides an interconnected space for vapour to pass through. Hence, the tortuosity of the pore channels will not change greatly under pressure, because there is sufficient space normal to the membrane surface for the filament to move without distorting the nominal channels.

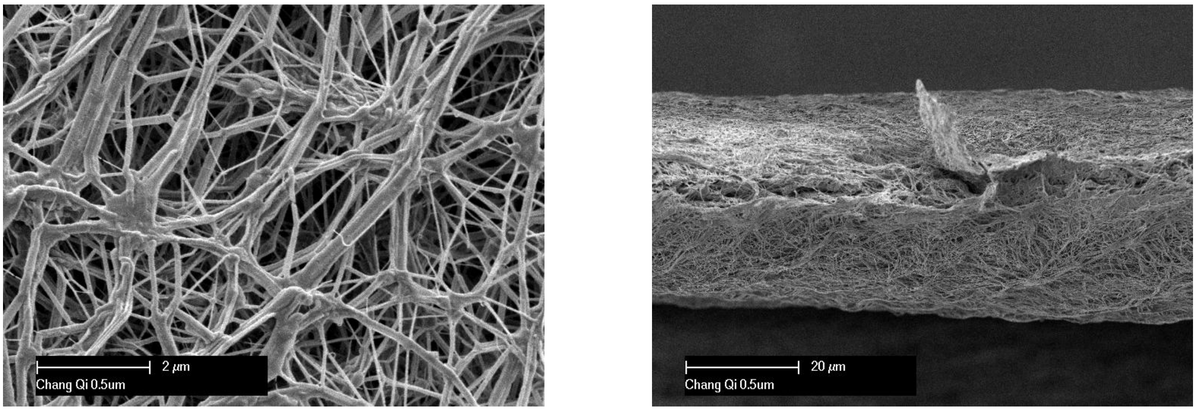

a. Surface of active layer

b. Cross section of active layer

Fig. 5 Images for membrane structure

4.2 Modelling and experimental results

4.2.1 Comparison of mathematical modelling results with experimental results

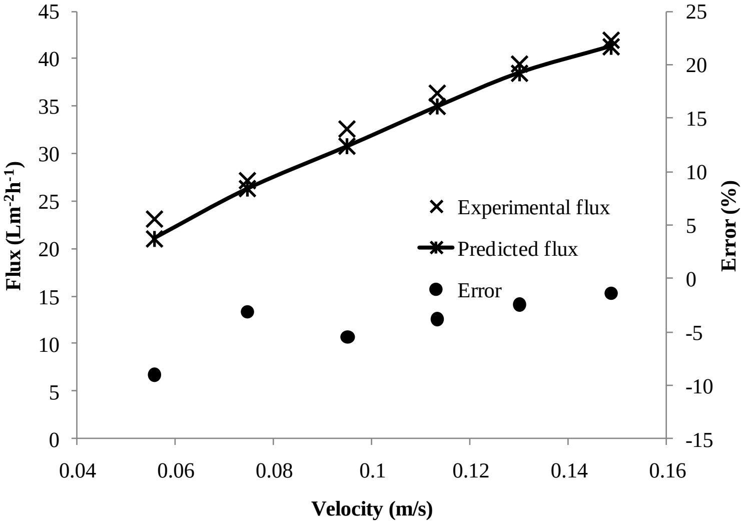

Fig. 6 Comparison between modelling and experimental flux at different velocities (T_{fi} = 60°C, T_{pi} = 20°C and L_{mem} = 130 mm)

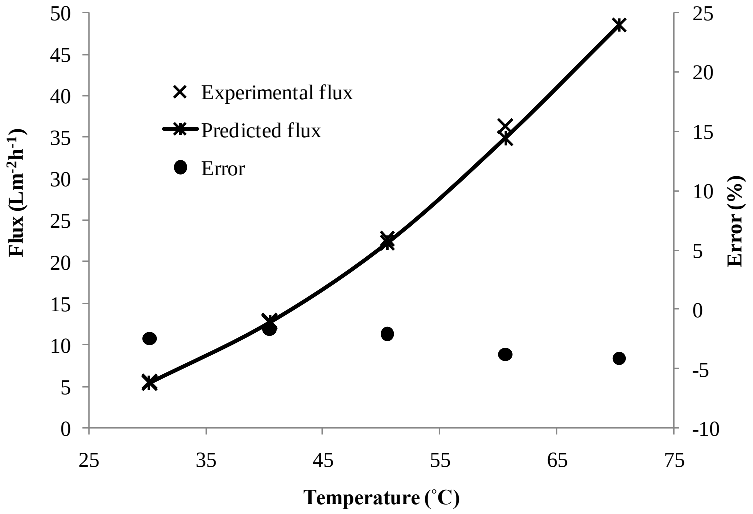

Fig. 7 Comparison between modelling and experimental flux results at different temperatures ($v_f = v_p$ =0.114 m/s, L_{mem} = 130 mm)

Fig. 6 shows the flux from experiments and model prediction at different velocities. The errors between the model predictions and the experimental results were in the range of -9 to -1.4%, and the maximum absolute errors occurred at the lowest velocity (0.056 $m.s^{-1}$).

Fig. 7 shows the similar results as those in Fig. 6 at different temperatures. The errors became larger at higher temperature, but they remain in the range of -4.1 to -1.7%. The maximum absolute error occurred at the highest temperature (70°C).

The model was also assessed with various membrane lengths. In Fig. 7, results from modelling and experiments are presented. The errors between the predicted and experimental results were randomly distributed in the range of -3.1 to 4.5%. The maximum absolute error was 4.5% with a membrane length of 0.733 m.

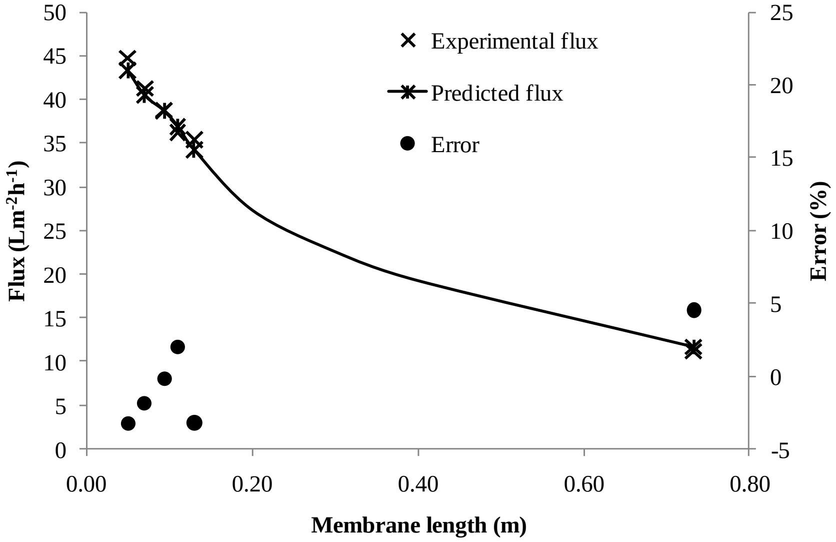

Fig. 8 Accuracy assessment with varied membrane lengths (T_{fi} = 60°C, T_{pi} =20°C, $v_f = v_p$ = 0.114 m/s)

Fig. 8 also shows that the flux decreases from 44.7 to 11.1 $L.m^{-2}h^{-1}$ as the membrane length was increased from 0.050 m to 0.733 m at the same inlet temperature and velocity. The decrease in flux results from the temperature profile change along the membrane module. As water evaporates and transfers from the hot brine to the cold permeate, heat is also transferred from the brine to the cold flow which reduces the temperature of the hot brine and increases the temperature of the cold flow. Thus, as the membrane length is increased, the mean temperature difference between the hot and cold sides reduces, which leads to a decrease in average flux. Therefore, the mass transfer coefficient (Eq. (19)) and $d\varepsilon/bt$ rather than the flux are better parameters to characterise membrane performance as these do not vary with membrane length or temperature.

The modelling results were also compared with experimental results under different pressures, because the PTFE membrane used was compressible. Fig. 9 shows the experimental and predicted flux values based on data from [2] , and errors between them under various pressures at different velocities and different hot inlet temperatures.

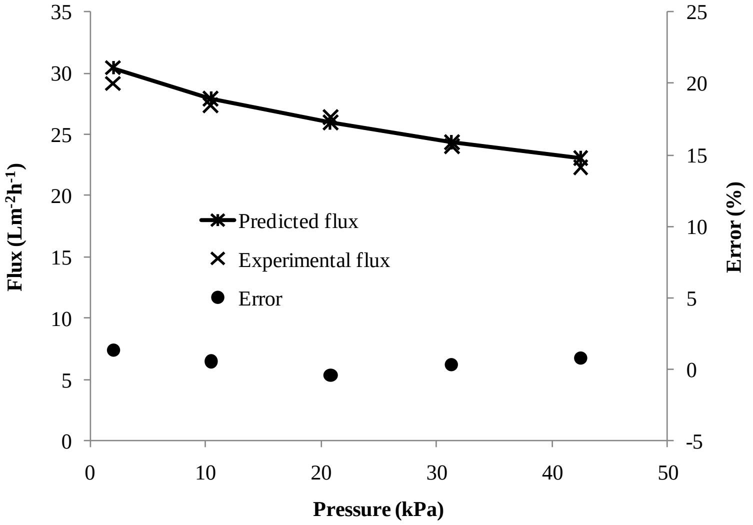

a. T_{fi} = 60°C, T_{pi} = 20°C, $v_f = v_p$ = 0.0945 m/s

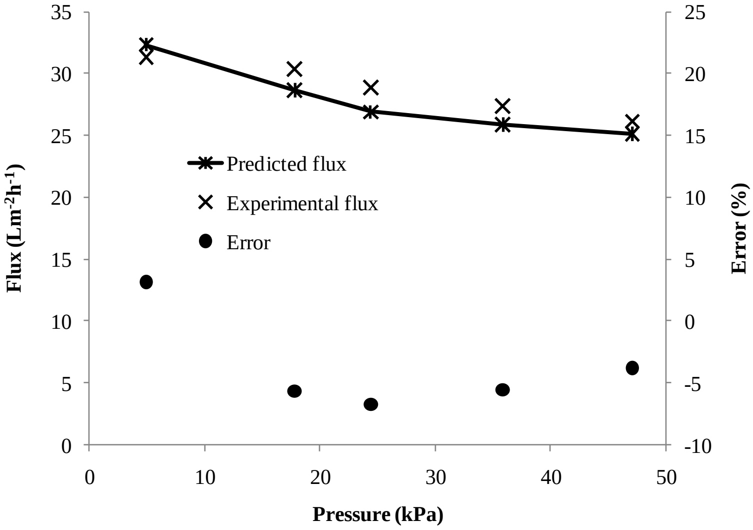

b. T_{fi} = 60°C, T_{pi} = 20°C, $v_f = v_p$ = 0.114 m/s

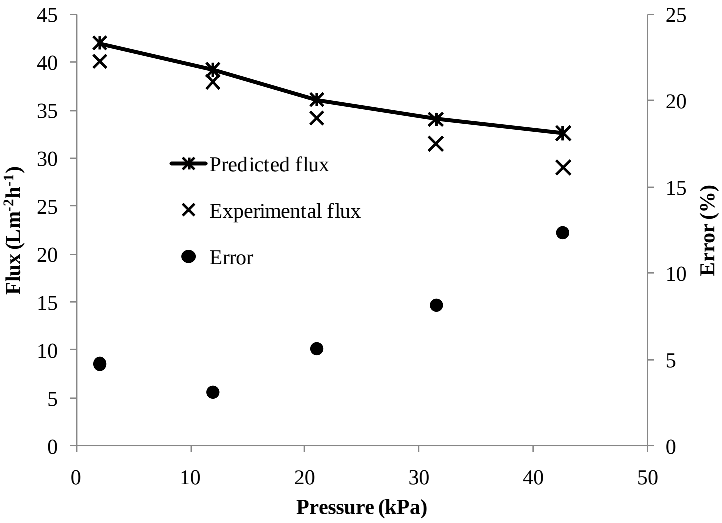

c. T_{fi} = 70°C, T_{pi} = 20°C, $v_f = v_p$ = 0.0945 m/s

Fig. 9 Prediction of model with various pressures under different conditions

It can be found from Fig. 9 that the flux decreased as the pressure applied on the membrane increased. Furthermore, the agreement between the model predictions and experimental results was very good when the feed inlet temperature was 60°C, for which the error was in the range of -2.1 to 1.3% at a velocity of 0.0945 m/s and -6.7 to 3.1% at a velocity of 0.114 m/s. This compares to an experimental variation of ±5%. The error was 3.1-12.4% (Fig. 9c) when the feed inlet temperature was 70°C at a velocity of 0.095 m/s. Unlike the other two sets of experiments, the modelling error at 70°C was not distributed randomly, and the greater errors occurred at high pressures (>30 kPa). The mean membrane mass transfer coefficients of these three membranes were estimated using the experimental data directly [2, 28] and are listed in Table 3, based on the assumptions listed in the paper of Zhang, et al. [2] .

Table 3

Estimated mean mass transfer coefficients under different pressures

Pressure range (kPa)	0-5	10-20	20-30	30-40	40-50
C_{m1} ($Lm^{-2}h^{-1}Pa^{-1}$)	0.0086	0.0088	0.0099	0.0097	0.0100
C_{m2} ($Lm^{-2}h^{-1}Pa^{-1}$)	0.0086	0.0101	0.0123	0.0129	0.0130
C_{m3} ($Lm^{-2}h^{-1}Pa^{-1}$)	0.0080	0.0113	0.0141	0.0145	0.0138

In Table 3, C_{m1}, C_{m2} and C_{m3} are respectively the mean mass transfer coefficients of membranes used for the experiments with hot inlet temperature of 70°C and velocity 0.0945 m/s, hot inlet temperature 60°C and velocity of 0.0945 m/s and hot inlet temperature 60°C and velocity of 0.114 m/s. Although the estimated C_{m1}, C_{m2} and C_{m3} were different from the local mass transfer coefficient in Eq. (19) which was calculated from the measured membrane properties, C_{m1}, C_{m2} and C_{m3} were still able to represent the membrane property changes with pressure. From Table 3, all three membranes had similar initial mass transfer coefficients (the membrane was selected for the experiments according to its initial flux. In this table, the membrane used for a higher temperature (at 70°C) had the smallest increase of C_{m1} with the pressure increment than that of the other two membranes. It was speculated that the compressibility of the membrane may be affected by temperature.

To verify this assumption, additional compressibility measurements were performed at elevated temperatures using the technique described in [2] but adapted for measurement at higher temperatures as outlined in the experimental section. Fig. 10 shows the compressibility of the membrane at 60°C (approximately the average interface temperature at the feed inlet temperature of 70°C for the experimental results shown in Fig. 9c), 45°C (approximately the interface temperature at the feed inlet temperature of 60°C for the experimental results shown in Figs. 9a,b) and 21°C (at which thickness changes with pressure used in the modelling program was measured [2]), respectively. This figure shows that the compressibility of the PTFE membrane employed depended on temperature. At 45ºC, the compressibility of membrane was approximately similar to that at the 21ºC, while a much greater compressibility was measured at 60 ºC. However, the calculated pressure in the pores at 60°C based on the volume change was greater than the pressure actually applied on the membrane, so the modelling program was not applicable at this temperature under pressure higher than 20 kPa. It is speculated that more water may have protruded into the membrane pores due to the reduced water surface tension and enlarged pore size (membrane expansion) at high temperature [29], leading to relative less thickness change. However, further study is needed to verify this assumption.

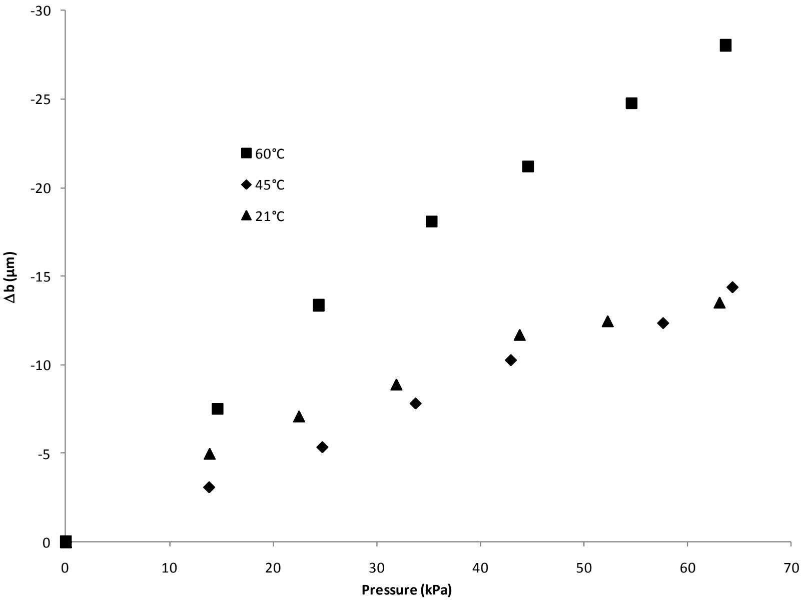

Fig. 10 Compressibility of membrane at different temperature

4.2.2 Effect of pressurised membrane on flux and temperature polarisation

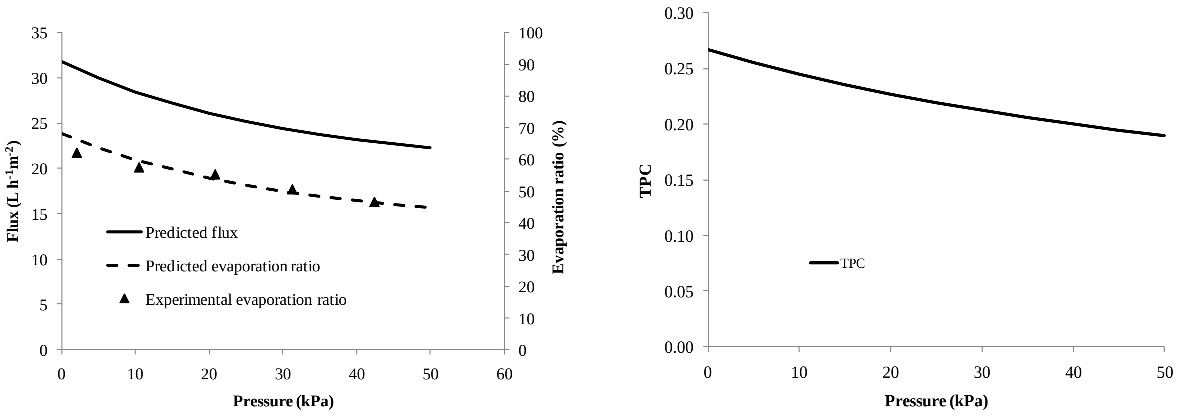

a. Flux and evaporation ratio b. TPC

Fig. 11 Influence of the pressure

(L_{mem} = 131 mm, T_{fi} = 60˚C, T_{pi} = 20˚C, $v_f = v_p$ = 0.0945 m/s)

For the compressible membrane, both the flux and evaporation ratio decreased as the pressure increases (Fig. 11a), and the TPC slightly reduced (Fig. 11b). Therefore, as the pressure applied on the compressible membrane increased, less heat was used for evaporation and the temperature polarisation increased. Thus, it is necessary to reduce the pressure drop along the module if a compressible membrane is employed in DCMD processes, e.g., reducing the membrane length in the flowing direction. Increasing the membrane dimension transverse to the flow rather than in the flow direction will reduce the flux loss during scale up.

4.2.3 Error analysis

Although the modelling results fitted the experimental results very well in most cases, on occasions the error was quite large (12.4%) due to the different compressibility behaviour of membrane at high temperature. The sources of the error could be:

A. Positive error (Overestimating the flux)
   - Ignoring the influence of feed concentration will lead to overestimating the vapour pressure at the feed interface and cause positive errors, which would be worse at low stream velocity (less mixing effect across the boundary layer) or high temperature (high concentration in the boundary layer due to quick evaporation), and
   - Ignoring heat loss through the module will also cause higher predicted feed interface temperature than that at the experimental conditions, which also would be worse at high temperature and low velocity, due to more heat loss for per unit mass,
   - Underestimating the compressibility of the membrane with pressure by not accounting for softening of PTFE at higher temperatures.

B. Negative error (underestimating the flux)
   - The parallel model for calculating thermal conductivity of the membrane active layer and the ignored difference of the latent heat across the pores of a membrane could overestimate the heat loss from the feed. At low velocity (long residency time) and high temperature (exponential relationship between temperature and flux), these assumptions will have more effect on predicted flux.

C. Uncertain error
   - Both negative and positive errors of modelling could occur, due to the variation of the membrane properties with the specific membrane section used.

5. Conclusions

A mathematical model capable of predicting the flux for flat sheet DCMD process under different pressures was developed based on the mass and heat transfer balances and the assumption of unchanged tortuosity with membrane compression.

The model predictions were compared with experimental results at different temperatures, velocities, membrane lengths and pressures, and showed reasonable agreement with experimental results at low feed inlet temperature (60˚C). However, although the error was less than 12.4% at a feed inlet temperature of 70˚C, the modelling program used for lower temperature was not applicable, because the compressibility of the membrane varied greatly at this temperature, and the equations correlating the thermal conductivity and permeability of the membrane with applied pressure were not reliable.

For spacer filled channels, the model used the local Nusselt number calculated from turbulent flow which provided a better fit to the experimental results than using an average Nusselt number along the membrane.

The modelling results suggest that in scaling up DCMD processes using compressible membranes, it is necessary to reduce the pressure drop along the module, e.g., reduce the membrane length in the flow direction.

Nomenclature

α_f, α_p	heat transfer coefficient on feed side and permeate side
A	membrane area
b	membrane thickness
$C_{membrane}$	membrane mass transfer coefficient
C_{pp}, C_{pf}	specific heat of water on permeate and feed sides
d	mean pore diameter of the membrane
ϕ	filament diameter
d_h	hydraulic diameter
D_{AB}	the diffusivity of water vapour (A) relative to air (B)
E	evaporation ratio
ε	membrane porosity
ε_{spacer}	spacer porosity
g	acceleration due to gravity
h_s	spacer thickness
H_g	enthalpy of vapour
$h_{f,i}$, $h_{p,i}$	enthalpies of the feed and permeate
J	vapour flux through the membrane
J_m, J_k	vapour flux through membrane pore arising from molecular and Knudsen diffusion
Kn	Knudsen number
K_s	spacer factor
l	mean molecular free path
L_{mem}	membrane length
λ	thermal conductivity of membrane
λ_{air} and λ_m	thermal conductivities of air and membrane material
$\dot{m}_f, \dot{m}_p$	mass velocity on the hot and permeate sides
M	the molecular weight of water
N_0	nominal pore number per square meter
Nu	Nusselt number
P	total pressure in the pore
P_A	partial vapour pressure in the pore

P_r	Prandtl number
P_{T1}, P_{T2}	vapour pressure at T_1 and T_2
Q	heat transfer
θ	angle between filament
R	universal gas constant
Re	Reynolds number
τ	pore tortuosity
T	mean temperature in the pore
T_f, T_p	bulk temperatures of feed and permeate
T_{fi}, T_{pi}	inlet and outlet temperatures of feed and permeate
T_1, T_2	feed and permeate temperatures at liquid-vapour interface
TPC	temperature polarisation coefficient
$V_{filament}$, V_{spacer}	filament and total volumes of spacer
V_{void}, V_a	void volume and total volume of the active layer
x	distance from feed inlet
x_A	mole fraction of water vapour in the pore
W	membrane width

References

[1] M. Tomaszewska, Membrane Distillation-Examples of Applications in Technology and Environmental Protection, Environmental Studies. 9(2000) 27-36.

[2] J. Zhang, J.-D. Li, S. Gray, Effect of applied pressure on performance of PTFE membrane in DCMD, Journal of Membrane Science. 369(2011) 514-525.

[3] F. Laganà, G. Barbieri, E. Drioli, Direct contact membrane distillation: modelling and concentration experiments, Journal of Membrane Science. 166(2000) 1-11.

[4] L. Song, B. Li, K. K. Sirkar, J. L. Gilron, Direct Contact Membrane Distillation-Based Desalination: Novel Membranes, Devices, Larger-Scale Studies, and a Model, Ind. Eng. Chem. Res. 46(2007) 2307-2323.

[5] L. Song, Z. Ma, X. Liao, P. B. Kosaraju, J. R. Irish, K. K. Sirkar, Pilot plant studies of novel membranes and devices for direct contact membrane distillation-based desalination, Journal of Membrane Science. 323(2008) 257-270.

[6] S. P. Agashichev, D. V. Falalejev, Modeling temperature polarization phenomena for longitudinal shell-side flow in membrane distillation process, Desalination. 108(1997) 99-103.

[7] Y. A. Cengel, M. A. Boles, Thermodynamics: an engineering approach. 6th ed., McGraw-Hill, New York, 2008.

[8] S. Bonyadi, T. S. Chung, Flux enhancement in membrane distillation by fabrication of dual layer hydrophilic-hydrophobic hollow fiber membranes, Journal of Membrane Science. 306(2007) 134-146.

[9] K. W. Lawson, D. R. Lloyd, Membrane distillation, Journal of Membrane Science. 124(1997) 1-25.

[10] J. Zhang, N. Dow, M. Duke, E. Ostarcevic, J.-D. Li, S. Gray, Identification of material and physical features of membrane distillation membranes for high performance desalination, Journal of Membrane Science. 349(2010) 295-303.

[11] M. C. Garcia-Payo, M. A. Izquierdo-Gil, Thermal resistance technique for measuring the thermal conductivity of thin microporous membranes, Journal of Physics D: Applied Physics. 37(2004) 3008-3016.

[12] J. Phattaranawik, R. Jiraratananon, A. G. Fane, Heat transport and membrane distillation coefficients in direct contact membrane distillation, Journal of Membrane Science. 212(2003) 177-193.

[13] M. Khayet, Membranes and theoretical modeling of membrane distillation: A review, Advances in Colloid and Interface Science. 164(2011) 56-88.

[14] R. W. Schofield, A. G. Fane, C. J. D. Fell, Heat and mass transfer in membrane distillation, Journal of Membrane Science. 33(1987) 299-313.

[15] A. O. Imdakm, T. Matsuura, A Monte Carlo simulation model for membrane distillation processes: direct contact (MD), Journal of Membrane Science. 237(2004) 51-59.

[16] Z. Ding, R. Ma, A. G. Fane, A new model for mass transfer in direct contact membrane distillation, Desalination. 151(2003) 217-227.

[17] A. M. Alklaibi, N. Lior, Membrane-distillation desalination: Status and potential, Desalination. 171(2005) 111-131.

[18] J. Phattaranawik, R. Jiraratananon, A. G. Fane, Effect of pore size distribution and air flux on mass transport in direct contact membrane distillation, Journal of Membrane Science. 215(2003) 75-85.

[19] Z. Lei, B. Chen, Z. Ding, Membrane distillation, in: Z. Lei, B. Chen, Z. Ding (Z. Lei, B. Chen, Z. Dings), Special Distillation Processes, Elsevier Science, Amsterdam, 2005, pp. 241-319.

[20] J. Woods, J. Pellegrino, J. Burch, Generalized guidance for considering pore-size distribution in membrane distillation, Journal of Membrane Science. 368(2011) 124-133.

[21] K. Schneider, T. J. van Gassel, Membrandestillation, Chemie Ingenieur Technik. 56(1984) 514-521.

[22] J. Phattaranawik, R. Jiraratananon, A. G. Fane, Effects of net-type spacers on heat and mass transfer in direct contact membrane distillation and comparison with ultrafiltration studies, Journal of Membrane Science. 217(2003) 193-206.

[23] J. H. I. Lienhard, J. H. V. Lienhard, A Heat Transfer Textbook. 3rd ed., Phlogiston Press, Cambridge, Massachusetts, U.S.A., 2003.

[24] A. L. Lydersen, Fluid Flow and Heat Transfer John Wiley & Sons Ltd, New York, 1979.

[25] J. Welty, C. E. Wicks, R. E. Wilson, G. L. Rorrer, Fundamentals of Momentum, Heat and Mass Transfer 3rd ed., John Wiley & Sons Inc, New York, 1984.

[26] J. Phattaranawik, R. Jiraratananon, A. G. Fane, C. Halim, Mass flux enhancement using spacer filled channels in direct contact membrane distillation, Journal of Membrane Science. 187(2001) 193-201.

[27] A. G. Fane, R. W. Schofield, C. J. D. Fell, The efficient use of energy in membrane distillation, Desalination. 64(1987) 231-243.

[28] M. Gryta, M. Tomaszewska, Heat transport in the membrane distillation process, Journal of Membrane Science. 144(1998) 211-222.

[29] J. Zhang, J.-D. Li, M. Duke, Z. Xie, S. Gray, Performance of asymmetric hollow fibre membranes in membrane distillation under various configurations and vacuum enhancement, Journal of Membrane Science. 362(2010) 517-528.

Modelling heat and mass transfers in DCMD using compressible membranes

Jianhua Zhang[a], Stephen Gray[a], Jun-De Li[a, b*]

[a]*Institute of Sustainability and Innovation, Victoria University, PO Box 14428, Melbourne, Victoria 8001, Australia*

[b]*School of Engineering and Science, Victoria University, PO Box 14428, Melbourne, Victoria 8001, Australia*

**Corresponding author, Tel.: +61-3-9919 4105, E-mail: jun-de.li@vu.edu.au*

Abstract

A model for predicting the flux and evaporation ratio in Direct Contact Membrane Distillation (DCMD) using a compressible membrane is presented. Polytetrafluoroethylene (PTFE) membranes, one of the most common types of membranes employed in MD, are characterised with high porosity (~90%) and high hydrophobicity, and therefore have high water vapour permeability and high wetting resistance. However, the PTFE membrane is compressible due to its structure. Compression of the membrane will cause a change of its physical structure, such as porosity, thickness, and pore size. As a result, the thermal conductivity and vapour permeability of the membrane will be altered, causing a change in flux and energy efficiency. Such effects need to be accounted for when scaling up from laboratory data to full scale design, because there may be significant differences in the applied pressure. Therefore, in this paper, the influence of pressure on the flux of the compressible PTFE membrane was modelled. This paper also provides a mathematical method to correlate the applied pressures with physical structure changes based on the assumption of constant tortuosity. The modelling results were compared with experimental results over a range of variable process parameters, i.e., temperatures, velocities, membrane lengths, and pressure applied to the membrane. The errors between the model predictions and experimental results were less than 10% within the operating range used in this investigation.

Keywords:

Direct contact membrane distillation, desalination, flux modelling, compressible membrane

1. Introduction

Membrane distillation (MD) is a membrane-based separation process, for which the driving force of separation is a vapour pressure difference across the membrane. The vapour pressure difference arises because of either a temperature difference across the membrane or a reduced vapour pressure on one side of the membrane. In comparison with other thermal desalination processes, the path length of vapour transport in MD is much smaller than that for multi-stage flash, multi-effect distillation and vapour compression, and is approximately the same as the membrane thickness (~100 μm). MD can also be used to treat high concentration or supersaturated solutions, because its driving force is not as sensitive to salt concentration as is the case for Reverse Osmosis (RO) [1, 2]. The capability of utilising low grade heat makes it possible to combine with solar heating, or sources of waste heat from power stations, chemical plants and other industries, to produce high purity water.

The characteristics of MD [1] membranes are: microporous, unwetted by process liquid, and do not altering the vapour equilibrium of different components in the process liquids. Additionally the MD process requires that no capillary condensation occurs inside the membrane pores, only the gas phase is able to pass through the pores, and the driving force for mass transfer is the partial pressure gradient across the membrane. In comparison with other desalination methods, MD has advantages such as: a nearly complete rejection of non-volatile components, a low operating pressure that is not related to feed concentration as is the case for reverse osmosis (RO), a simple structure and operation, a small vapour space, and low operating temperatures (40-80°C) [1]. These characteristics make it a promising technique for desalination where low grade heat is available, such as in industrial sites. Furthermore, high salinity wastewater, such as the concentrate from RO processes, is difficult to treat by RO because of the high osmotic pressure and the presence of scaling compounds. MD could be used after RO to recover additional water from the concentrate streams and thus reduce the volume of brine for disposal.

In our MD pilot plant using compressible flat sheet PTFE membrane, a dramatic flux decrease was found in comparison with laboratory scale results under similar operating conditions. This reduction of flux was greater than the predicted flux reduction if only changes in length were considered. It was expected that the pressure drop would be much higher in the flow channel of the pilot/industry scale module than the laboratory scale module, due to longer flow channels. It was also found in our research that the performance of the compressible membrane was related to the pressure applied on its surface [2] in MD. Former MD modelling [3] has mainly focused on membranes with constant properties that are unaffected by pressure. However, as compressible membranes are subjected to external pressure, the physical properties, such as thickness, pore size and porosity are altered, so as to cause the changes of its thermal conductivity and permeability. In this paper, the pore size, porosity, thickness and thermal conductivity of the membrane are not considered as constants but are varied with applied pressure. Although the relationship between the flux and membrane length was included in the modelling for hollow fibre DCMD [4-6], it was rarely considered for the flat sheet modules with spacer filled channels.

1.1 Heat transfer

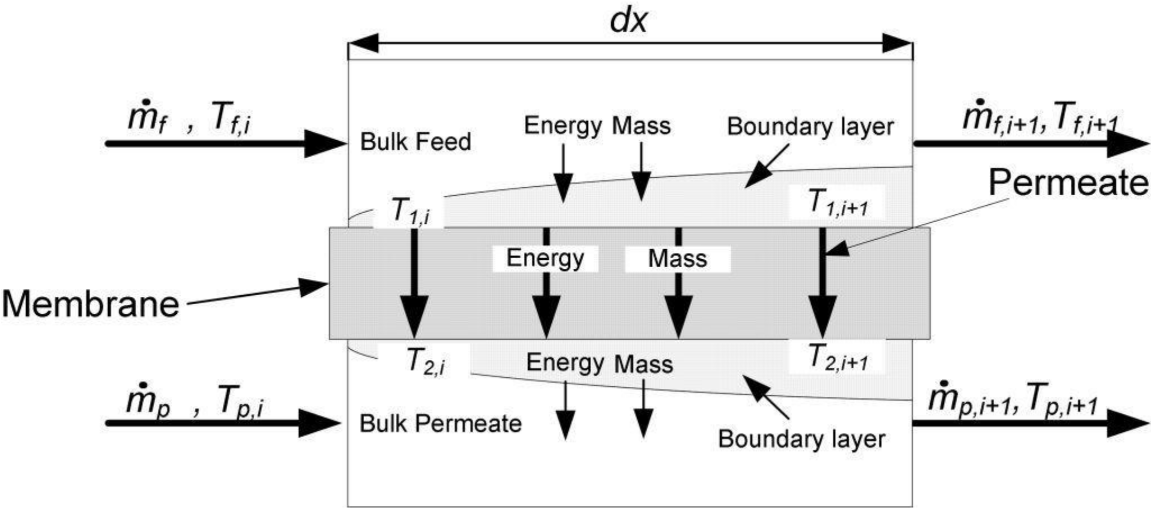

Fig.1 Heat and mass transfer through the membrane

In DCMD, the driving force for mass transfer is the vapour pressure difference that arises from the temperature difference between the liquids on both sides of the membrane. Thus, DCMD performance relies on the complex relationships between simultaneous heat and mass transfers, which are in the same direction from the feed side to the permeate side. In Fig. 1, *dx* is the length of the small element which is located at a distance *x* from the inlet of the hot feed, and the subscript *i* is the i^{th} element from $x = 0$. Based on Fig. 1, for the feed side:

$$Q_{f,transfer} = \alpha_f (T_f - T_1) W dx \tag{1}$$

For permeate side:

$$Q_{p,transfer} = \alpha_p (T_2 - T_p) W dx \tag{2}$$

where $Q_{f,transfer}$ is the absolute overall heat transfer, W is the width of the membrane, and T_1 and T_2 are the interface temperatures at the interfaces of the membrane with the feed and permeate streams. The heat transfer through the membrane is:

$$Q_{f,transfer} = \left(\frac{\lambda}{b}(T_1 - T_2) + JH_{g,T1}\right)Wdx, \text{ or}$$

$$Q_{p,transfer} = \left(\frac{\lambda}{b}(T_1 - T_2) + JH_{g,T2}\right)Wdx \tag{3}$$

where H_g is the enthalpy of the vapour, λ is the thermal conductivity of the membrane, b is the membrane thickness and J is the flux

Supposing the difference between T_1 and T_2 is as great as 40°C, the enthalpy difference of the vapour (60 °C and 20°C) is about 71 kJ/kg [7], which is only 3% of the enthalpy of vapour at 20°C. If the average vapour enthalpy in the pore is used, the difference will be only about 1% of the enthalpy of vapour at 20°C. If a temperature polarisation coefficient (TPC) of 0.5 (in our work the highest TPC < 0.35) is applied, the temperature difference of T_1 and T_2 should be less than 20°C, and the enthalpy difference between the average enthalpy and the enthalpy at T_1 and T_2 will be less than 0.5%. Therefore, it can be assumed that:

$$\bar{H}_{g,pore} \approx H_{g,T1} \approx H_{g,T2} \tag{4}$$

It can be deduced that [8, 9]:

$$Q_{f,transfer} \approx \left(\frac{\lambda}{b}(T_1 - T_2) + J\bar{H}_g\right)Wdx \approx Q_{p,transfer} \tag{5}$$

where $\bar{H}_g$ is the enthalpy of the vapour in the pore.

In Eq. (5), $\lambda(T_1\text{-}T_2)/b$ is the sensible heat transfer across the membrane and $J\bar{H}_g$ is heat transfer accompanying the mass transfer. Therefore, the evaporation ratio (expressed in percentage) used for evaporation (E) can be defined as [10]:

$$E = \frac{J\bar{H}_g}{Q_{f,transfer}} \times 100\% \tag{6}$$

The heat transfers across the feed, membrane and permeate should be in balance, and thus:

$$\alpha_f(T_f - T_1)Wdx = \left(\frac{\lambda}{b}(T_1 - T_2) + J\bar{H}_g\right)Wdx = \alpha_p(T_2 - T_p)Wdx \tag{7}$$

The thermal conductivity in this paper was initially measured experimentally using a similar method to Garcia-Payo and Izquierdo-Gil [11]. This method required placing the membrane between two copper plates and measuring the heat flow between the copper plates. However, it was found the results were not reliable, because it was difficult to make perfect contact between the compressible membrane and the copper discs without compressing the membrane. Therefore, it is difficult to conclude if the measured thermal conductivity was overestimated (if the membrane was compressed) or underestimated (if contact was not good).

For the calculation of thermal conductivity of porous membranes, studies [11, 12] have determined mathematic models to fit experimental results. In these papers, a method to ensure good contact between the membrane and copper discs was mentioned, but there was no discussion of whether this contact caused deformation of the membrane, especially for the PTFE membranes studied. Therefore, these models may be not applicable for the PTFE compressible membranes used in this study. Furthermore, the tortuosity factor of the employed PTFE membrane was about 1.1 [2]. This indicates that the pore channels were approximately straight and perpendicular to the membrane surface, so it can be speculated that the pores and the solid walls between the pores were aligned almost parallel. Therefore, a conservative and popular parallel model [8, 9, 13] in MD modelling was to calculate the thermal conductivity of the active layer as

$$\lambda_{active} = \lambda_{air}\varepsilon + \lambda_{solid}(1 - \varepsilon) \tag{8}$$

where λ_{active}, λ_{air} and λ_{solid} are the thermal conductivities of the active layer, air and the solid material, respectively, and ε is the membrane porosity.

The TPC [14] for DCMD is normally used to access the process efficiency of DCMD and is defined as:

$$TPC = \frac{T_1 - T_2}{T_f - T_p} \tag{9}$$

1.2 Mass transfer in DCMD

The hydrophobic MD membrane is a porous medium. The mass transfer through such medium can be interpreted by three kinds of basic mechanisms: Knudsen diffusion, molecular diffusion and Poiseuille flow [15]. The Knudsen number (*Kn*)

$$Kn = l/d \tag{10}$$

is used to evaluate the dominating mechanism of the mass transfer in the pores. Here, *l* is the mean free path of the transferred gas molecules and *d* is the mean pore diameter of the membrane.

Table 1 shows the dominating mass transfer mechanism based on *Kn* in a gas mixture with a uniform pressure throughout the system [16].

Table 1
Mass transfer mechanism in membrane pore

Kn<0.01	0.01<*Kn*<1	*Kn*>1
molecular diffusion	Knudsen-molecular diffusion transition mechanism	Knudsen mechanism

As the pore size of the MD membranes is in general in the range of 0.2-1.0 µm [17] and the mean free path of the water vapour is 0.11 µm at a feed temperature of 60°C [18], *Kn* calculated from Eq. (10) is in the range of 0.55-0.11. Therefore, Knudsen-molecular transition diffusion is the dominating mass transfer mechanism within the pores, irrespective of pore size distribution of the membrane [18, 19]. Therefore, the overall mass flux across the membrane can be expressed as:

$$\frac{1}{J} = \frac{1}{J_k} + \frac{1}{J_m} = \frac{1}{\frac{4}{3} d \frac{\varepsilon}{b\tau} \sqrt{\frac{1}{2\pi RMT}} \Delta P} + \frac{1}{\left(\frac{1}{1 - x_A} \cdot \frac{\varepsilon}{b\tau} \cdot \frac{D_{AB}}{RT} \right) \Delta P} \tag{11}$$

where J_m and J_k are the vapour flux through the membrane arising from molecular and Knudsen diffusion, τ is the pore tortuosity factor, R is the universal gas constant, M is the molecular mass of the vapour, D_{AB} is the diffusivity of water (A) to air (B), x_A is the mole fraction of water in the pore and P_{T1} and P_{T2} are the vapour pressures at temperature T_1 and T_2, which can be calculated by the Antoine equation [20].

2. Theory

2.1 Variation of membrane properties with pressure

Mass transfer of compressed membranes

In Eq. (11), the diffusivity (D_{AB}) of water vapour (A) relative to air (B) can be modelled in membrane distillation as [19, 21]:

$$D_{AB} = \frac{1.895 \times 10^{-5} T^{2.072}}{P} \tag{12}$$

In this study, as the absolute pressure (100- 160 kPa) in the pores is low, the water vapour and air in the pores can be assumed an ideal gas mixture. Therefore, the mole fraction of the water vapour x_A can be calculated as:

$$x_A = \frac{P_A}{P} \tag{13}$$

So the total vapour flux across the membrane shown in Eq. (11) can be derived as:

$$J = 7.81 \times \frac{\varepsilon d}{b\tau} \frac{MT^{1.072}}{5.685\sqrt{2\pi RMT} + 4dR(P - P_A)} (P_{T1} - P_{T2}) \tag{14}$$

As the membrane is compressed, it has been shown [8] that the thickness of the active layer is reduced. As a result, the pore size, porosity and tortuosity are expected to change. As the active membrane layer considered in this work was a uniform membrane (ie. non-asymmetric) with a coarse, porous scrim support, the porosity can be calculated as:

$$\varepsilon = \frac{V_{void}}{V_a} = \frac{N_0 \frac{\pi d^2}{4} b \tau^{0.5}}{b} = N_0 \frac{\pi d^2 \tau^{0.5}}{4} \qquad (15)$$

where N_0 is the nominal number of pores per square meter in the active layer, and V_{void}, and V_a are the void volume and total volume of the active layer, respectively. In Eq. (15), we have assumed that the pores are cylindrical. Because porosity and pore size can be measured by the methods provided in [2], N_0 can be estimated by:

$$N_0 = \frac{4\varepsilon_0}{\pi d_0^2 \tau_0^{0.5}} \qquad (16)$$

Here subscript 0 is for membrane under no compression. Under the assumption that N_0 does not change with pressure, using the changes in membrane thickness and porosity with pressure determined experimentally, the pore size under different pressures can be calculated by:

$$d_p = \sqrt{\frac{4\varepsilon_p}{N_0 \pi \tau_p^{0.5}}} \qquad (17)$$

where ε_p, τ_p and d_p are the porosity, tortuosity factor and pore diameter of the membrane at pressure P. In Eq. (17), the change of tortuosity factor (τ_p) with pressure is unknown for the employed PTFE membrane, but was assumed that it does not change greatly for the pressure range considered , i.e. it is assumed $\tau_p = \tau_0$. This assumption was based on a calculated tortuosity factor around 1.1 [2], i.e. the pores were almost vertically aligned, and the pressure applied normally will not distort the pores in the direction normal to the membrane greatly. Therefore, the compression of the membrane does not affect the ratio of pore length to membrane thickness (tortuosity) greatly, as the pore length is almost equal to the membrane thickness.

The total flux of a membrane under pressure can thus be expressed as:

$$J = 7.81 \times \frac{\varepsilon \sqrt{\frac{4\varepsilon_p}{N_0 \pi \tau_0^{0.5}}}}{b \tau_0} \frac{M T^{1.072}}{5.685\sqrt{2\pi R M T} + 4\sqrt{\frac{4\varepsilon_p}{N_0 \pi \tau_0^{0.5}}} R (P - P_A)} (P_{T1} - P_{T2}) \qquad (18)$$

Eq. (18) can also be simplified to:

$$J_p = C_{membrane,p} (P_{T1} - P_{T2}) \qquad (19)$$

where $C_{membrane,p}$ is the mass transfer coefficient of the membrane under pressure.

Thermal conductivity of the compressed membrane

As shown in Eq. (8), the thermal conductivity of the membrane is related to the porosity. For a compressed membrane, the porosity decreases so the thermal conductivity of the membrane increases. Since the porosity change with pressure is experimentally measurable, the variation of thermal conductivity of the active layer with pressure can be estimated via Eq. (8) [2]. The thermal conductivity of the whole membrane was calculated by adding the thermal conductivities of the scrim layer and the active layer in series.

2.2 Theoretical analyses of the heat transfer and mass transfer

When developing a model for heat and mass transfer across the membranes, the following assumptions were made:

- no heat loss through the module wall (< 1% estimated heat loss of the feed),

- the heat of vaporisation and condensation does not change with concentration, because low concentration feed (1 wt%) was used, and no obvious difference between deionised water and this feed was found in the previous experiments,
- the tortuosity does not change with pressure,
- in balancing the heat transfer, variations in latent heat at different interface temperatures is ignored, and
- there is no temperature gradient across the width of the membrane (i.e. perpendicular to the flow direction.

To analyse the heat transfer between the hot feed and the cold permeate, a small element was considered as shown in the schematic diagram in Fig. 1. Based on Fig. 1, the energy balance equations for feed and permeate temperatures distributed along the membrane can be written as:

$\dot{m}_{f,i}h_{f,i} = \dot{m}_{f,i+1}h_{f,i+1} + Q_{transfer,i}$, and

$\dot{m}_{p,i}h_{p,i} + Q_{transfer,i} = \dot{m}_{f,i+1}h_{p,i+1}$ (20)

where $\dot{m}_f$ and $\dot{m}_p$ are the mass flow rates of the feed and permeate, and $h_{f,i}$ and $h_{p,i}$ are the enthalpies of the feed and permeate.

Due to the mass transfer across the membrane, the mass flow rates of the feed and permeate are related as:

$\dot{m}_{f,i} = \dot{m}_{f,i+1} + J_i W dx$, and

$\dot{m}_{p,i} + J_i W dx = \dot{m}_{p,i+1}$ (21)

By using the $Q_{f,transfer}$ and $Q_{p,transfer}$ from Eqs. (1) and (2), the temperature of the feed and permeate at *i+1* can be calculated as:

$T_{f,i+1} = \frac{\dot{m}_{f,i}C_{p,f,i}T_{f,i} - \alpha_f(T_{f,i} - T_{1,i})Wdx}{C_{p,f,i+1}\dot{m}_{f,i+1}}$, and

$T_{p,i+1} = \frac{\dot{m}_{f,i}C_{p,p,i}T_{p,i} + \alpha_p(T_{p,i} - T_{1,i})Wdx}{C_{p,p,i+1}\dot{m}_{p,i+1}}$ (22)

where $C_{p,f}$ and $C_{p,p}$ are the specific heats of the feed and permeate.

3. Experiment and simulation

3.1 Membrane characterisation

Membrane materials were provided by Changqi Co. Ltd and consisted of a polytetrafluoroethylene (PTFE) active layer and a polypropylene (PP) scrim support layer. The nominal pore size was 0.5 µm.

SEM characterisation

The active layer, support layer and the cross section (thickness) of the membrane were observed by a Philips XL30 FEG Scanning Electron Microscope (SEM). The membrane was fractured following immersion in liquid nitrogen to form an intact cross section [10] before it was scanned.

Air permeability measurement

The pore size of the membrane and $d_0\varepsilon_0/b_0\tau_0$ were estimated by the gas permeability method [19] using compressed nitrogen and by varying the pressure in the range of 5-80 kPa. The pressure difference across the membrane, at the same distance from the feed inlet, was set at 1.00±0.01 kPa. A digital manometer (645, TPI) was used to measure the pressure and the pressure difference. A stopwatch was used to record the time. Five samples from the different parts of a membrane were tested, and the average value was used in subsequent analysis. A schematic drawing of the apparatus is shown in Fig. 2.

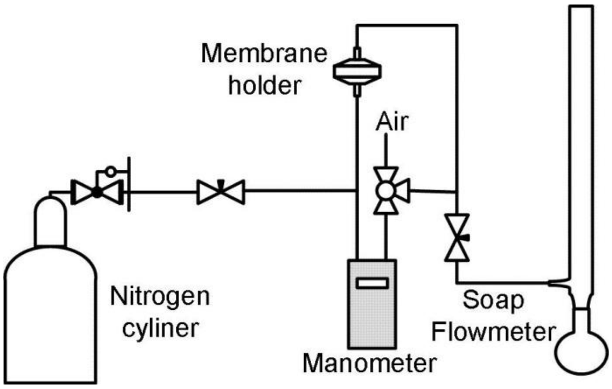

Fig. 2 Air permeability testing instrument

Measurement for porosity, thickness and compressibility

The porosity and thickness of the membrane under different pressures were measured with the method provided in [2]. When the thickness of the membrane as a function of pressure was measured at elevated temperatures, the pressurised chamber was placed in a water bath and the temperature stabilised over several hours before measurements were taken to guarantee no air bubbles occurs, and a blank test was also done under the same operation conditions.

3.2 Experimental process

Experiments under different conditions were performed to verify the model. A schematic diagram of the DCMD process is shown in Fig. 3.

For the experiments performed under low pressure (0 - 3 kPa), the pressure control valves were fully open. The velocities of the feed and permeate streams were varied from 0.055 to 0.151 m/s (300-800 mL/min), and the feed and permeate streams were maintained at the same velocity in all experiments using two peristaltic pumps. The flowrate was calibrated using a volumetric cylinder and the accuracy was ±10 mL/min. Two digitally controlled water baths (refrigerated and heated) were used to control the inlet temperatures of the permeate at 20±2°C and the feed in the range of 30-70±2°C. The brine feed was prepared by dissolving 50 g NaCl in 5 L water (10 g.L^{-1}). Four temperature sensors were used to measure the temperatures of the hot brine and cold permeate streams at their inlets and outlets. A conductivity meter in the product reservoir was used to monitor changes in conductivity, which were used to calculate salt rejection and to monitor for leaks. Flux was determined by measuring the weight of the product reservoir over time and was calculated based on the membrane area. The membrane length was varied in the range of 50-130 mm. A larger module with an active membrane size of 200×733 mm was also used to verify the model.

The experiments with pressure applied on the membranes were described in Zhang et. al [2]. Four series of experiments were performed including two series in which the pressure was varied at the velocities of 0.0945 and 0.114 m/s (520 and 620 mL/min) at hot and cold inlet temperatures of 60 and 20°C, respectively. For the other two series the pressure was varied for hot stream inlet temperatures of 50 and 70±2°C at velocities of 0.0945 m/s. All experiments were conducted with identical pressures in the feed and permeate streams and the pressures varied from 3 to 45±3 kPa.

All flux results were measured over a period of 2.5 to 4 hours and the variation in flux (calculated every half or one hour) over this time was ±5%. Most experiments were repeated under the same conditions, variations of flux were found in the range of ±5% when different portions of a membrane were employed. Except for data presented in the figure showing the influence of membrane length on flux, all the data presented in each figure were from a piece of new membrane. Before the membranes were used, they were conditioned for 3 h at feed and permeate inlet temperatures of 60 and 20°C and velocity of 0.0945 m/s with pressure control valves fully opened.

In the conditioning period (no membrane compression), only the membranes with initial flux falling into the range of ±5% of the average flux were selected for further experiments.

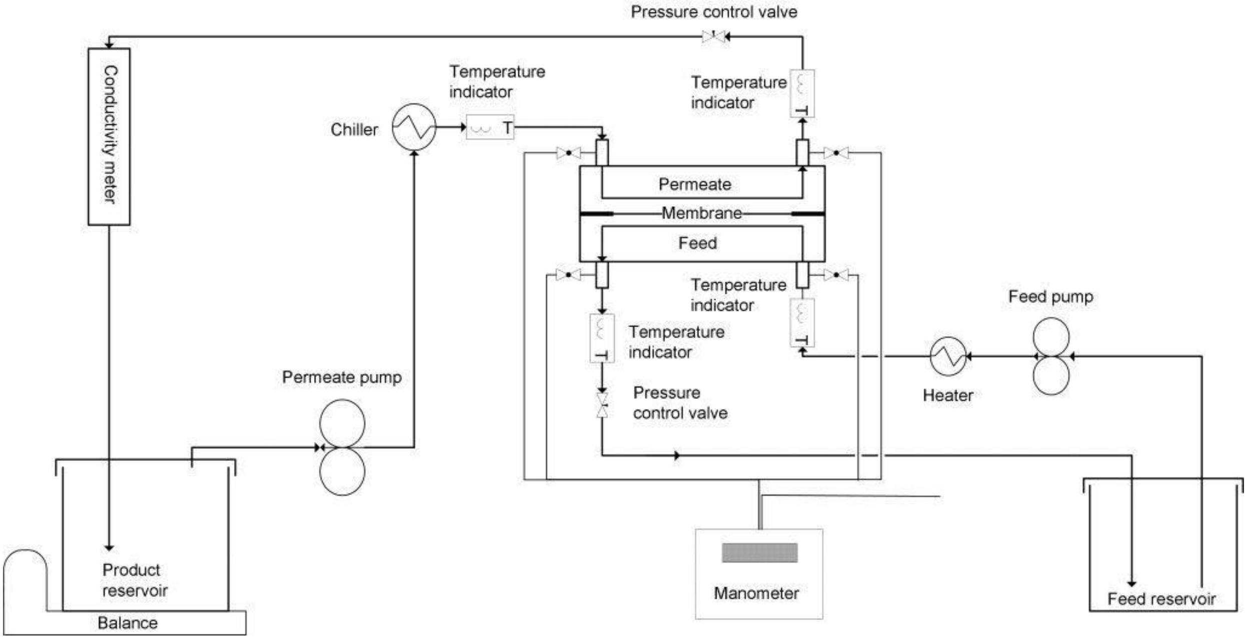
Pressure control valve
Conductivity meter
Temperature indicator
Chiller
T
Temperature indicator
T
Permeate
Membrane
Feed
Temperature indicator
T
Temperature indicator
T
Feed pump
Heater
Pressure control valve
Permeate pump
Product reservoir
Balance
Manometer
Feed reservoir

Fig. 3 Schematic diagrams of the employed DCMD process

3.3 Modelling heat and mass transfer for spacer filled channel

The spacer used was 0.8 mm thick and composed of filaments (ϕ = 0.4 mm), as shown in Fig. 4. The spacer was used to support the membrane and it also acted as a turbulence promoter. The spacer porosity was measured experimentally and calculated using [10],

$$\varepsilon_{spacer} = \frac{V_{filament}}{V_{spacer}} \tag{23}$$

where ε_{spacer} is the porosity of the spacer, $V_{filament}$ is the volume of spacer filament and V_{spacer} is the total spacer volume.

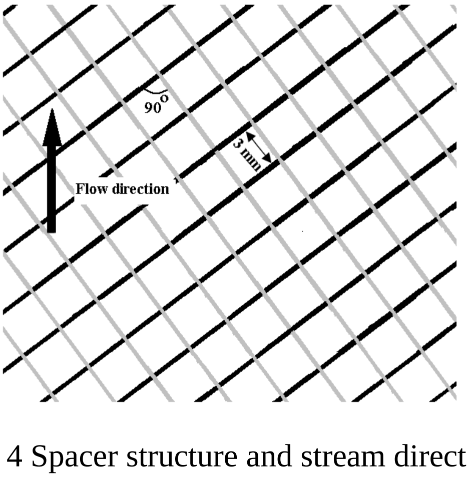
90°
3 mm
Flow direction

Fig. 4 Spacer structure and stream direction

Because temperature varies as the hot and cold streams flow along the DCMD module, water properties (viscosity, saturated vapour pressure and latent heat) need to be calculated at each location along the membrane length to account for the change in temperature. Therefore, a Nusselt number (*Nu*) that varied with the local temperature was used for the calculation of convective heat transfer coefficient, rather than a Nusselt number using average temperature as used in [21]. From the Nusselt number, the local convective heat transfer coefficients (α_f, α_p) can be calculated [22].

For the spacer filled channel, although the Reynolds number was less than 300, the model predictions fit the experimental data better when an approximate solution recommended by [23, 24] of *Nu* on a flat surface of fully developed turbulent flow was used in the modelling:

$$Nu = 0.0292Re^{0.8}Pr^{0.33} \qquad (24)$$

For the spacer filled channel, the Nusselt number needed to be calibrated by a spacer factor K_s [21, 25],

$$Nu_s = K_s Nu \qquad (25)$$

where K_s is the spacer factor:

$$K_s = a\left(\frac{\phi}{h_s}\right)^c \varepsilon_{spacer}^d \left(\sin\frac{\theta}{2}\right)^e \qquad (26)$$

where θ is the angle between filaments as shown in Fig. 4 and h_s is the thickness of the spacer. In this work, a = 1.9, c = 0.039, d = 0.75, and e = 0.086 are coefficients mainly from the work of Phattaranawik, J. al et. [25], except for a which is 1.15 times the value the given in [25]. The coefficient a was adjusted based on the experiment with stream velocities at 0.114 m/s and membrane length of 0.13 m, and inlet temperatures of feed and permeate of 60˚C and 20°C, and it was verified with different stream velocities, temperatures, membrane lengths and pressures.

3.4 Numerical solution

The DCMD flow channel in the module was divided into small elements *dx*, and solved numerically. This numerical solution was implemented using MATLAB.

For counter-current flows, $x = 0$ was taken at the inlet of the hot feed and the mass flowrate on the cold permeate side was taken as a negative value. An iteration procedure was used to solve the system of equations [26].

Based on Eq. (7), the membrane interface temperatures $T_{1,j}$ and $T_{2,j}$ were calculated by first determining the overall heat transfer using [19]:

$$Q_{f,transfer,i} \approx Q_{p,transfer,i} = \frac{T_{f,i} - T_{p,i} + J_i H_{g,i}\left(\frac{b}{\lambda}\right)}{\frac{1}{\alpha_{f,ij}} + \frac{1}{\alpha_{p,i}} + \frac{b}{\lambda}} W dx \qquad (27)$$

For given flowrates and geometry, the heat and mass transfer coefficients at $x = x_i$ were calculated using Eq. (9) and the bulk temperatures $T_{f,i+1}$ and $T_{p,i+1}$ were obtained. From Eqs. (1) and (2), these can be approximated as:

$$T_{1,i+1} = T_{f,i} - \frac{Q_{f,transfer,i}}{\alpha_{f,i}} \qquad (28)$$

$$T_{2,i+1} = \frac{Q_{p,transfer,i}}{\alpha_{p,i}} + T_{p,i} \qquad (29)$$

For the $(i+1)^{th}$ element, the mass flow rate on the feed side is reduced and that on the permeate sides is increased due to the vaporisation, so the feed and permeate bulk temperatures were calculated using Eq. (22).

4. Results and discussion

4.1 Analytical results and discussion

Table 2 lists the measured and calculated membrane properties. The mean pore size measured by the gas permeation was similar to the nominal pore size provided by the manufacturer (0.5 μm).

Table 2
Properties of PTFE membrane

d_0 (μm)	ε_0 (%)	b_0 (μm)	$d_0\varepsilon_0/b_0\tau_0$ ($\times10^{-3}$)	τ_0	λ_0/b_0 ($W\cdot K^{-1}\cdot m^{-2}$)	N_0 ($\times10^{12}\ m^{-2}$)
0.5±0.08	91±0.5	46±1	8.7±0.7	1.08±0.03	980±40	4.0±0.2

The deformation of the compressible PTFE membrane under different pressures was reported in [2].

The structures of the active layer are shown in Fig. 5. The images show that the PTFE active layer has a web like structure, so that it is very difficult to determine the pore size directly by visualisation, as there were no obvious pores. The stretching-formed filament structure provides an interconnected space for vapour to pass through. Hence, the tortuosity of the pore channels will not change greatly under pressure, because there is sufficient space normal to the membrane surface for the filament to move without distorting the nominal channels.

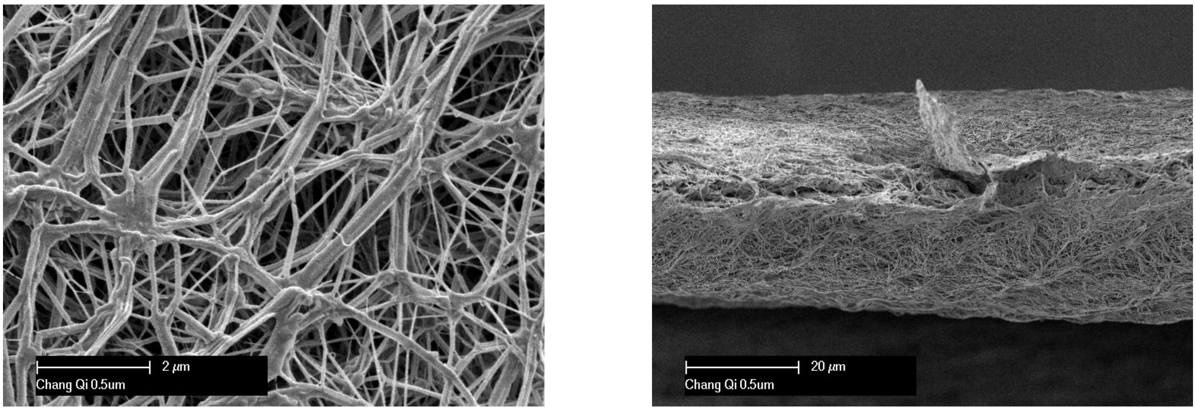

a. Surface of active layer

b. Cross section of active layer

Fig. 5 Images for membrane structure

4.2 Modelling and experimental results

4.2.1 Comparison of mathematical modelling results with experimental results

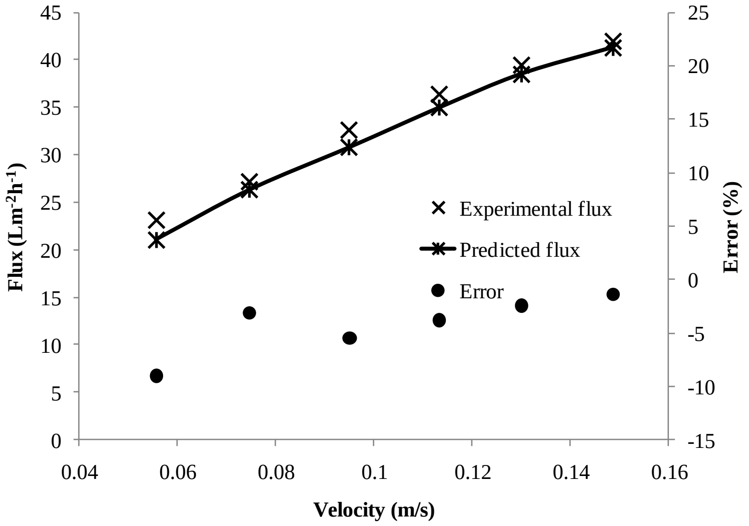

Fig. 6 Comparison between modelling and experimental flux at different velocities (T_{fi} = 60°C, T_{pi} = 20°C and L_{mem} = 130 mm)

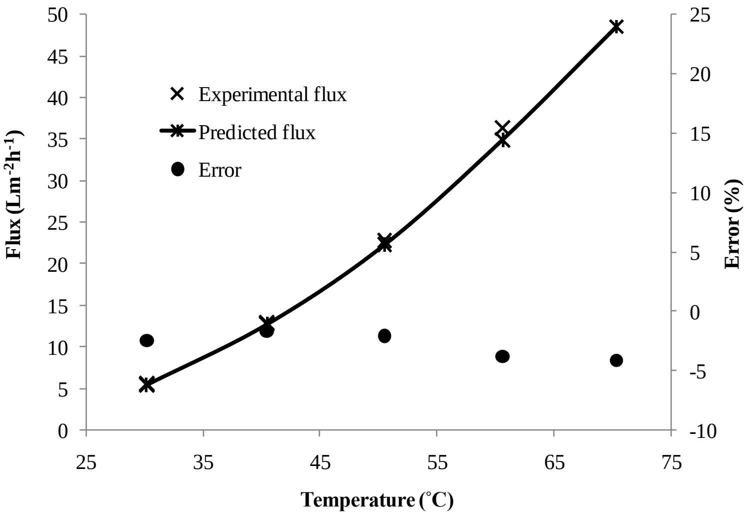

Fig. 7 Comparison between modelling and experimental flux results at different temperatures ($v_f = v_p$ =0.114 m/s, L_{mem} = 130 mm)

Fig. 6 shows the flux from experiments and model predictions at different velocities. The errors between the model predictions and the experimental results were in the range of -9 to -1.4%, and the maximum absolute errors occurred at the lowest velocity (0.056 m.s^{-1}).

Fig. 7 shows the similar results as those in Fig. 6 at different temperatures. The errors became larger at higher temperature, but they remain in the range of -4.1 to -1.7%. The maximum absolute error occurred at the highest temperature (70°C).

The model was also assessed with various membrane lengths. In Fig. 8, results from modelling and experiments are presented. The errors between the predicted and experimental results were randomly distributed in the range of -3.1 to 4.5%. The maximum absolute error was 4.5% with a membrane length of 0.733 m.

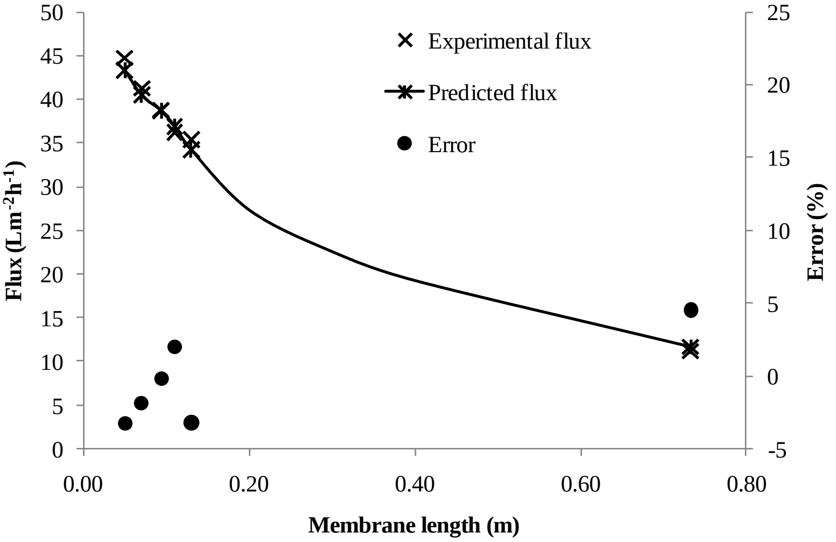

Fig. 8 Accuracy assessment with varied membrane lengths (T_{fi} = 60°C, T_{pi} =20°C, $v_f = v_p$ = 0.114 m/s)

Fig. 8 also shows that the flux decreases from 44.7 to 11.1 L.m^{-2}h^{-1} as the membrane length was increased from 0.050 m to 0.733 m at the same inlet temperature and velocity. The decrease in flux results from the temperature profile change along the membrane module. As water evaporates and transfers from the hot brine to the cold permeate, heat is also transferred from the brine to the cold flow which reduces the temperature of the hot brine and increases the temperature of the cold flow.

Thus, as the membrane length is increased, the mean temperature difference between the hot and cold sides reduces, which leads to a decrease in average flux. Therefore, the mass transfer coefficient (Eq. (19)) and *dε/bt* rather than the flux are better parameters to characterise membrane performance as these do not vary with membrane length or temperature.

The modelling results were also compared with experimental results under different pressures, because the PTFE membrane used was compressible. Fig. 9 shows the experimental and predicted flux values based on data from [2] , and errors between them under various pressures at different velocities and different hot inlet temperatures.

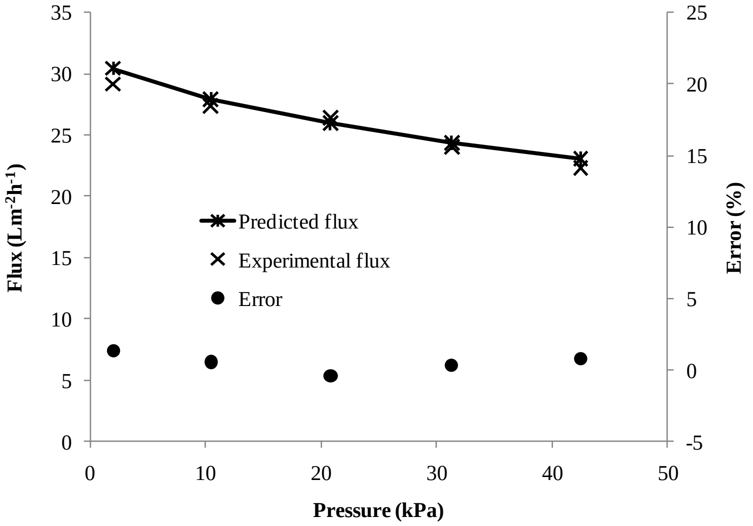

a. T_{fi} = 60°C, T_{pi} = 20°C, $v_f = v_p$ = 0.0945 m/s

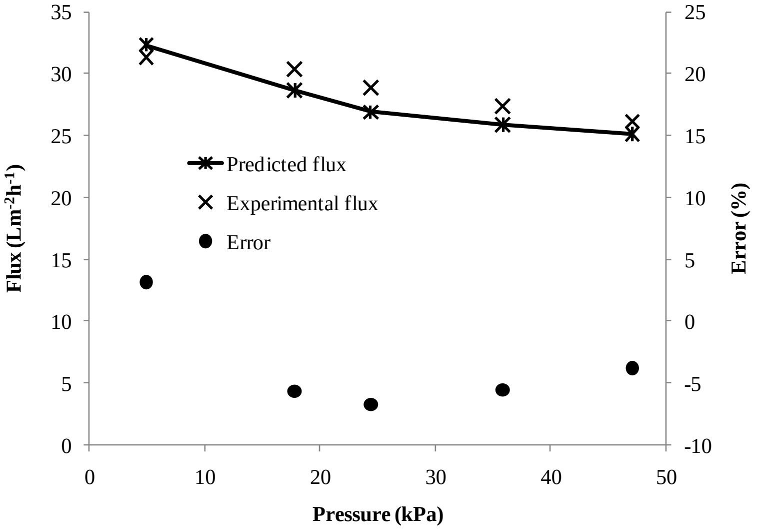

b. T_{fi} = 60°C, T_{pi} = 20°C, $v_f = v_p$ = 0.114 m/s

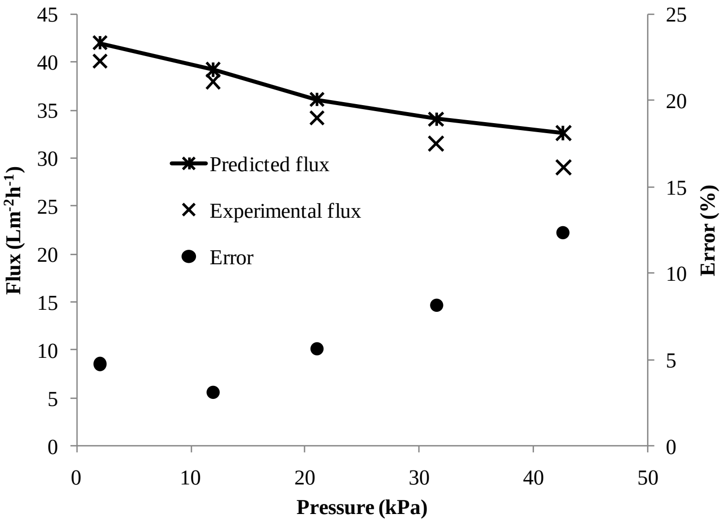

c. T_{fi} = 70°C, T_{pi} = 20°C, $v_f = v_p$ = 0.0945 m/s

Fig. 9 Prediction of model with various pressures under different conditions

It can be found from Fig. 9 that the flux decreased as the pressure applied on the membrane increased. Furthermore, the agreement between the model predictions and experimental results was very good when the feed inlet temperature was 60°C, for which the error was in the range of -2.1 to 1.3% at a velocity of 0.0945 m/s and -6.7 to 3.1% at a velocity of 0.114 m/s. This compares to an experimental variation of ±5%. The error was 3.1-12.4% (Fig. 9c) when the feed inlet temperature was 70°C at a velocity of 0.095 m/s. Unlike the other two sets of experiments, the modelling error at 70°C was not distributed randomly, and the greater errors occurred at high pressures (>30 kPa). The mean membrane mass transfer coefficients of these three membranes were estimated using the experimental data directly [2, 27] and are listed in Table 3, based on the assumptions listed in the paper of Zhang, et al. [2] .

Table 3
Estimated mean mass transfer coefficients under different pressures

Pressure range (kPa)	0-5	10-20	20-30	30-40	40-50
C_{m1} ($Lm^{-2}h^{-1}Pa^{-1}$)	0.0086	0.0088	0.0099	0.0097	0.0100
C_{m2} ($Lm^{-2}h^{-1}Pa^{-1}$)	0.0086	0.0101	0.0123	0.0129	0.0130
C_{m3} ($Lm^{-2}h^{-1}Pa^{-1}$)	0.0080	0.0113	0.0141	0.0145	0.0138

In Table 3, C_{m1}, C_{m2} and C_{m3} are respectively the mean mass transfer coefficients of membranes used for the experiments with hot inlet temperature of 70°C and velocity 0.0945 m/s, hot inlet temperature 60°C and velocity of 0.0945 m/s and hot inlet temperature 60°C and velocity of 0.114 m/s. Although the estimated C_{m1}, C_{m2} and C_{m3} were different from the local mass transfer coefficient in Eq. (19) which was calculated from the measured membrane properties, C_{m1}, C_{m2} and C_{m3} were still able to represent the membrane property changes with pressure. From Table 3, all three membranes had similar initial mass transfer coefficients (the membrane was selected for the experiments according to its initial flux. In this table, the membrane used for a higher temperature (at 70°C) had the smallest increase of C_{m1} with the pressure increment among the three membranes. It was speculated that the compressibility of the membrane may be affected by temperature. Fig. 10

shows the compressibility of the membrane at 60°C (approximately the average interface temperature at the feed inlet temperature of 70°C), 45°C (approximately the the interface temperature at the feed inlet temperature of 60°C) and 21°C (at which thickness changes with pressure used in the modelling program was measured [2]). This figure shows that the compressibility of the PTFE membrane employed depended on temperature. At 45ºC, the compressibility of the membrane was approximately similar to that at 21ºC, while a much greater compressibility was measured at 60 ºC. However, the calculated pressure in the pores at 60°C based on the volume change was greater than the pressure actually applied on the membrane, so the modelling program was not applicable at this temperature under pressure higher than 20 kPa. It is possible that some water may protrude into the membrane pores due to the reduced water surface tension and enlarged pore size (membrane expansion) at high temperature [28], leading to the increase in apparent thickness change. Further study is needed to verify this assumption.

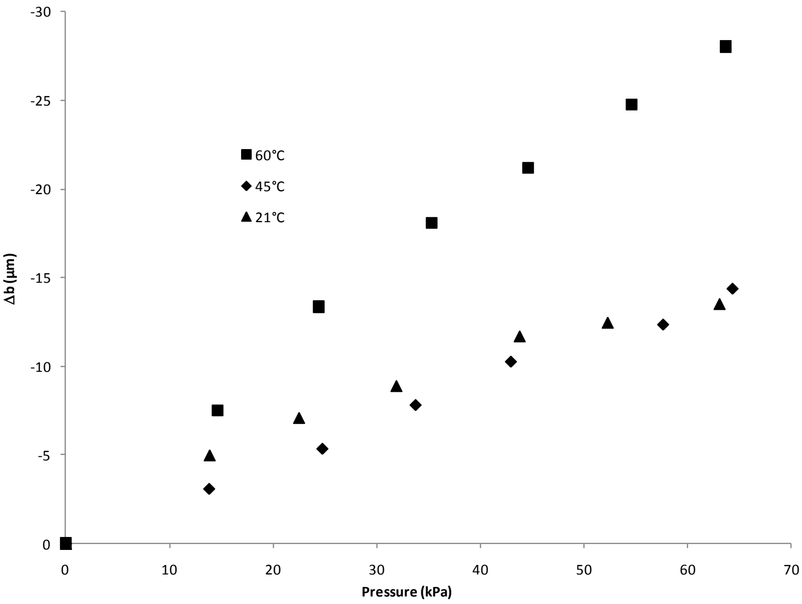

Fig. 10 Compressibility of membrane at different temperature

4.2.2 Effect of pressurised membrane on flux and temperature polarisation

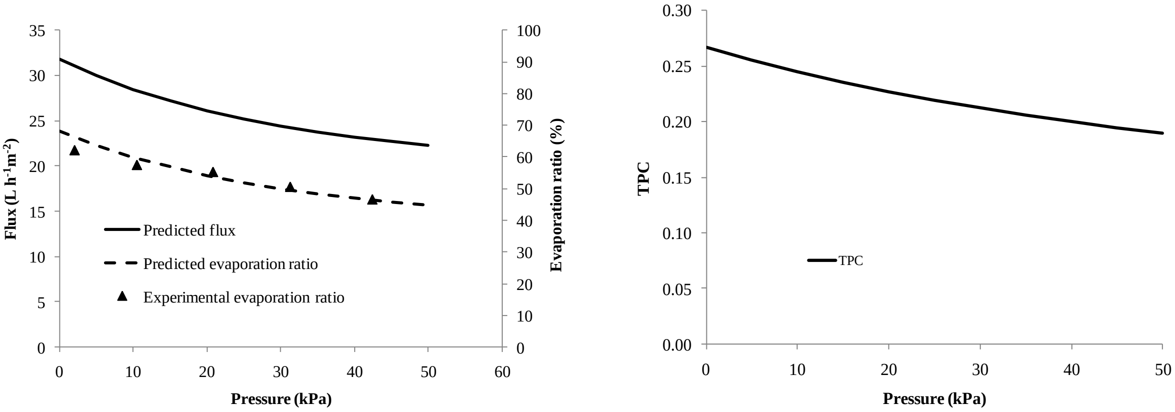

a. Flux and evaporation ratio b. TPC

Fig. 11 Influence of the pressure

(L_{mem} = 131 mm, T_{fi} = 60˚C, T_{pi} = 20˚C, $v_f = v_p$ = 0.0945 m/s)

For the compressible membrane, both the flux and evaporation ratio decreased as the pressure increases (Fig. 11a), and the TPC was slightly reduced (Fig. 11b). Therefore, as the pressure applied on the compressible membrane was increased, less heat was used for evaporation and the temperature polarisation increased. Thus, it is necessary to reduce the pressure drop along the module if a compressible membrane is employed in DCMD processes, e.g., reducing the membrane length in the flowing direction. Increasing the membrane dimension transverse to the flow rather than in the flow direction will reduce the flux loss during scale up.

4.2.3 Error analysis

Although the modelling results fitted the experimental results very well in most cases, on occasions the error was quite large (12.4%) due to the different compressibility behaviour of membrane at high temperature. The sources of the error could be:

A. Positive error (Overestimating the flux)
  - Ignoring the influence of feed concentration will lead to overestimating the vapour pressure at the feed interface and cause positive errors, which would be worse at low stream velocity (less mixing effect across the boundary layer) or high temperature (high concentration in the boundary layer due to quick evaporation), and
  - Ignoring heat loss through the module will also cause higher predicted feed interface temperature than that at the experimental conditions, which also would be worse at high temperature and low velocity, due to more heat loss for per unit mass,
  - Underestimating the compressibility of the membrane with pressure by not accounting for softening of PTFE at higher temperatures.

B. Negative error (underestimating the flux)
  - The parallel model for calculating thermal conductivity of the membrane active layer and the ignored difference of the latent heat across the pores of a membrane could overestimate the heat loss from the feed. At low velocity (long residency time) and high temperature (exponential relationship between temperature and flux), these assumptions will have more effect on predicted flux.

C. Uncertain error
  - Both negative and positive errors of modelling could occur, due to the variation of the membrane properties with the specific membrane section used.

5. Conclusions

A mathematical model capable of predicting the flux for flat sheet DCMD process under different pressures was developed based on the mass and heat transfer balances and the assumption of unchanged tortuosity with membrane compression.

The model predictions were compared with experimental results at different temperatures, velocities, membrane lengths and pressures, and showed reasonable agreement with experimental results at low feed inlet temperature (60˚C). Although the error was less than 12.4% at a feed inlet temperature of 70˚C, the modelling program used for higher temperature was not applicable, because the compressibility of the membrane varied greatly at this temperature, and the equations correlating the thermal conductivity and permeability of the membrane with applied pressure were not reliable.

For spacer filled channels, the model used the local Nusselt number calculated from turbulent flow which provided a better fit to the experimental results than using an average Nusselt number along the membrane.

The modelling results suggest that in scaling up DCMD processes using compressible membranes, it is necessary to reduce the pressure drop along the module, e.g., reduce the membrane length in the flow direction.

Nomenclature

α_f, α_p	heat transfer coefficient on feed side and permeate side
A	membrane area
b	membrane thickness
$C_{membrane}$	membrane mass transfer coefficient
C_{pp}, C_{pf}	specific heat of water on permeate and feed sides
d	mean pore diameter of the membrane
ϕ	filament diameter
d_h	hydraulic diameter
D_{AB}	the diffusivity of water vapour (A) relative to air (B)
E	evaporation ratio
ε	membrane porosity
ε_{spacer}	spacer porosity
g	acceleration due to gravity
h_s	spacer thickness
H_g	enthalpy of vapour
$h_{f,i}$, $h_{p,i}$	enthalpies of the feed and permeate
J	vapour flux through the membrane
J_m, J_k	vapour flux through membrane pore arising from molecular and Knudsen diffusion
Kn	Knudsen number
K_s	spacer factor
l	mean molecular free path
L_{mem}	membrane length
λ	thermal conductivity of membrane
λ_{air} and λ_m	thermal conductivities of air and membrane material
$\dot{m}_f,\dot{m}_p$	mass velocity on the hot and permeate sides
M	the molecular weight of water
N_0	nominal pore number per square meter
Nu	Nusselt number
P	total pressure in the pore
P_A	partial vapour pressure in the pore
P_r	Prandtl number
P_{T1}, P_{T2}	vapour pressure at T_1 and T_2
Q	heat transfer
θ	angle between filament
R	universal gas constant
Re	Reynolds number
τ	pore tortuosity
T	mean temperature in the pore
T_f, T_p	bulk temperatures of feed and permeate
T_{fi}, T_{pi}	inlet and outlet temperatures of feed and permeate
T_1, T_2	feed and permeate temperatures at liquid-vapour interface
TPC	temperature polarisation coefficient

$V_{filament}$, V_{spacer}	filament and total volumes of spacer
V_{void}, V_a	void volume and total volume of the active layer
x	distance from feed inlet
x_A	mole fraction of water vapour in the pore
W	membrane width

References

[1] M. Tomaszewska, Membrane Distillation-Examples of Applications in Technology and Environmental Protection, Environmental Studies. 9(2000) 27-36.

[2] J. Zhang, J.-D. Li, S. Gray, Effect of applied pressure on performance of PTFE membrane in DCMD, Journal of Membrane Science. 369(2011) 514-525.

[3] F. Laganà, G. Barbieri, E. Drioli, Direct contact membrane distillation: modelling and concentration experiments, Journal of Membrane Science. 166(2000) 1-11.

[4] L. Song, B. Li, K. K. Sirkar, J. L. Gilron, Direct Contact Membrane Distillation-Based Desalination: Novel Membranes, Devices, Larger-Scale Studies, and a Model, Ind. Eng. Chem. Res. 46(2007) 2307-2323.

[5] L. Song, Z. Ma, X. Liao, P. B. Kosaraju, J. R. Irish, K. K. Sirkar, Pilot plant studies of novel membranes and devices for direct contact membrane distillation-based desalination, Journal of Membrane Science. 323(2008) 257-270.

[6] S. P. Agashichev, D. V. Falalejev, Modeling temperature polarization phenomena for longitudinal shell-side flow in membrane distillation process, Desalination. 108(1997) 99-103.

[7] Y. A. Cengel, M. A. Boles, Thermodynamics: an engineering approach. 6th ed., McGraw-Hill, New York, 2008.

[8] S. Bonyadi, T. S. Chung, Flux enhancement in membrane distillation by fabrication of dual layer hydrophilic-hydrophobic hollow fiber membranes, Journal of Membrane Science. 306(2007) 134-146.

[9] K. W. Lawson, D. R. Lloyd, Membrane distillation, Journal of Membrane Science. 124(1997) 1-25.

[10] J. Zhang, N. Dow, M. Duke, E. Ostarcevic, J.-D. Li, S. Gray, Identification of material and physical features of membrane distillation membranes for high performance desalination, Journal of Membrane Science. 349(2010) 295-303.

[11] M. C. Garcia-Payo, M. A. Izquierdo-Gil, Thermal resistance technique for measuring the thermal conductivity of thin microporous membranes, Journal of Physics D: Applied Physics. 37(2004) 3008-3016.

[12] J. Phattaranawik, R. Jiraratananon, A. G. Fane, Heat transport and membrane distillation coefficients in direct contact membrane distillation, Journal of Membrane Science. 212(2003) 177-193.

[13] M. Khayet, Membranes and theoretical modeling of membrane distillation: A review, Advances in Colloid and Interface Science. 164(2011) 56-88.

[14] R. W. Schofield, A. G. Fane, C. J. D. Fell, Heat and mass transfer in membrane distillation, Journal of Membrane Science. 33(1987) 299-313.

[15] A. O. Imdakm, T. Matsuura, A Monte Carlo simulation model for membrane distillation processes: direct contact (MD), Journal of Membrane Science. 237(2004) 51-59.

[16] Z. Ding, R. Ma, A. G. Fane, A new model for mass transfer in direct contact membrane distillation, Desalination. 151(2003) 217-227.

[17] A. M. Alklaibi, N. Lior, Membrane-distillation desalination: Status and potential, Desalination. 171(2005) 111-131.

[18] J. Phattaranawik, R. Jiraratananon, A. G. Fane, Effect of pore size distribution and air flux on mass transport in direct contact membrane distillation, Journal of Membrane Science. 215(2003) 75-85.

[19] Z. Lei, B. Chen, Z. Ding, Membrane distillation, in: Z. Lei, B. Chen, Z. Ding (Z. Lei, B. Chen, Z. Dings), Special Distillation Processes, Elsevier Science, Amsterdam, 2005, pp. 241-319.

[20] K. Schneider, T. J. van Gassel, Membrandestillation, Chemie Ingenieur Technik. 56(1984) 514-521.

[21] J. Phattaranawik, R. Jiraratananon, A. G. Fane, Effects of net-type spacers on heat and mass transfer in direct contact membrane distillation and comparison with ultrafiltration studies, Journal of Membrane Science. 217(2003) 193-206.

[22] J. H. I. Lienhard, J. H. V. Lienhard, A Heat Transfer Textbook. 3rd ed., Phlogiston Press, Cambridge, Massachusetts, U.S.A., 2003.

[23] A. L. Lydersen, Fluid Flow and Heat Transfer John Wiley & Sons Ltd, New York, 1979.

[24] J. Welty, C. E. Wicks, R. E. Wilson, G. L. Rorrer, Fundamentals of Momentum, Heat and Mass Transfer 3rd ed., John Wiley & Sons Inc, New York, 1984.

[25] J. Phattaranawik, R. Jiraratananon, A. G. Fane, C. Halim, Mass flux enhancement using spacer filled channels in direct contact membrane distillation, Journal of Membrane Science. 187(2001) 193-201.

[26] A. G. Fane, R. W. Schofield, C. J. D. Fell, The efficient use of energy in membrane distillation, Desalination. 64(1987) 231-243.

[27] M. Gryta, M. Tomaszewska, Heat transport in the membrane distillation process, Journal of Membrane Science. 144(1998) 211-222.

[28] J. Zhang, J.-D. Li, M. Duke, Z. Xie, S. Gray, Performance of asymmetric hollow fibre membranes in membrane distillation under various configurations and vacuum enhancement, Journal of Membrane Science. 362(2010) 517-528.

Figure

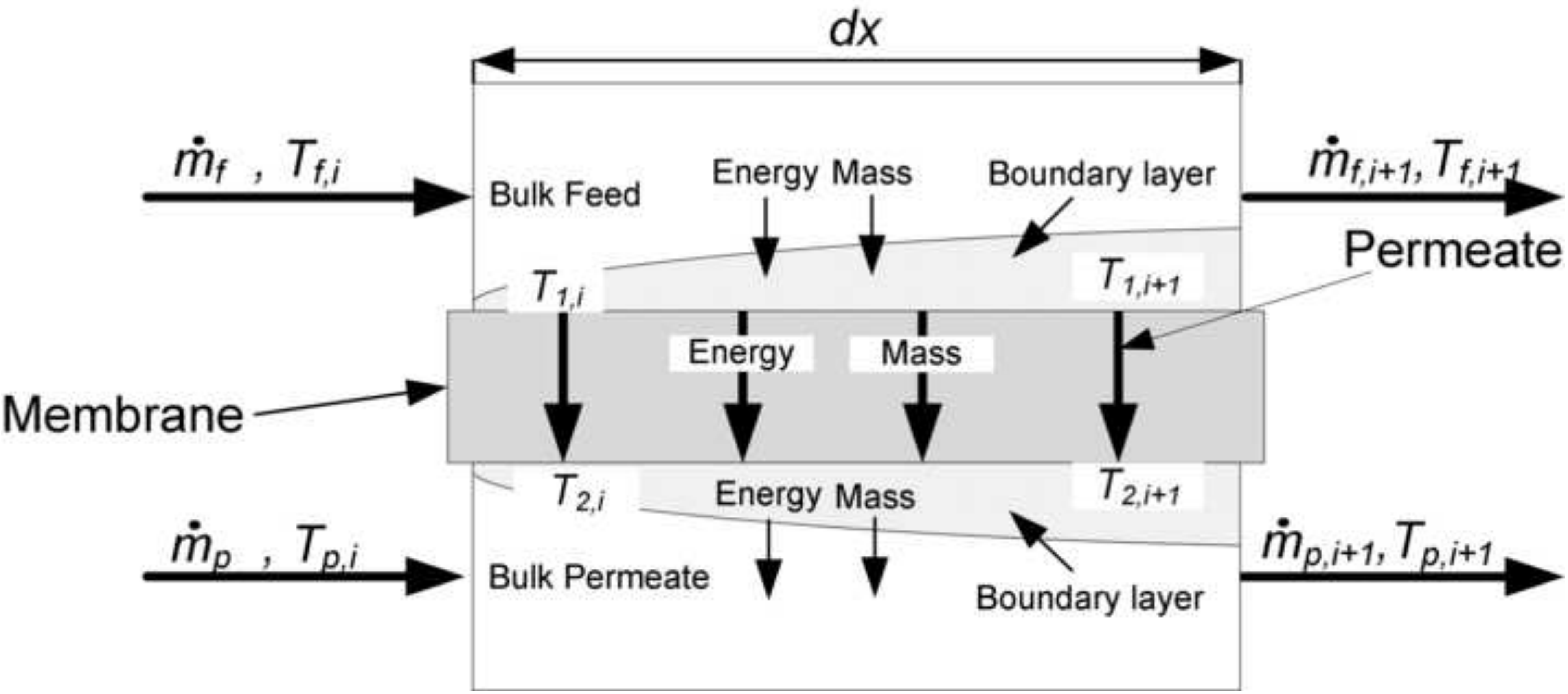

dx
$\dot{m}_f$, $T_{f,i}$
Bulk Feed
Energy Mass
Boundary layer
$\dot{m}_{f,i+1}, T_{f,i+1}$
Permeate
$T_{1,i}$
$T_{1,i+1}$
Energy
Mass
Membrane
$T_{2,i}$
Energy Mass
$T_{2,i+1}$
$\dot{m}_p$, $T_{p,i}$
Bulk Permeate
Boundary layer
$\dot{m}_{p,i+1}, T_{p,i+1}$

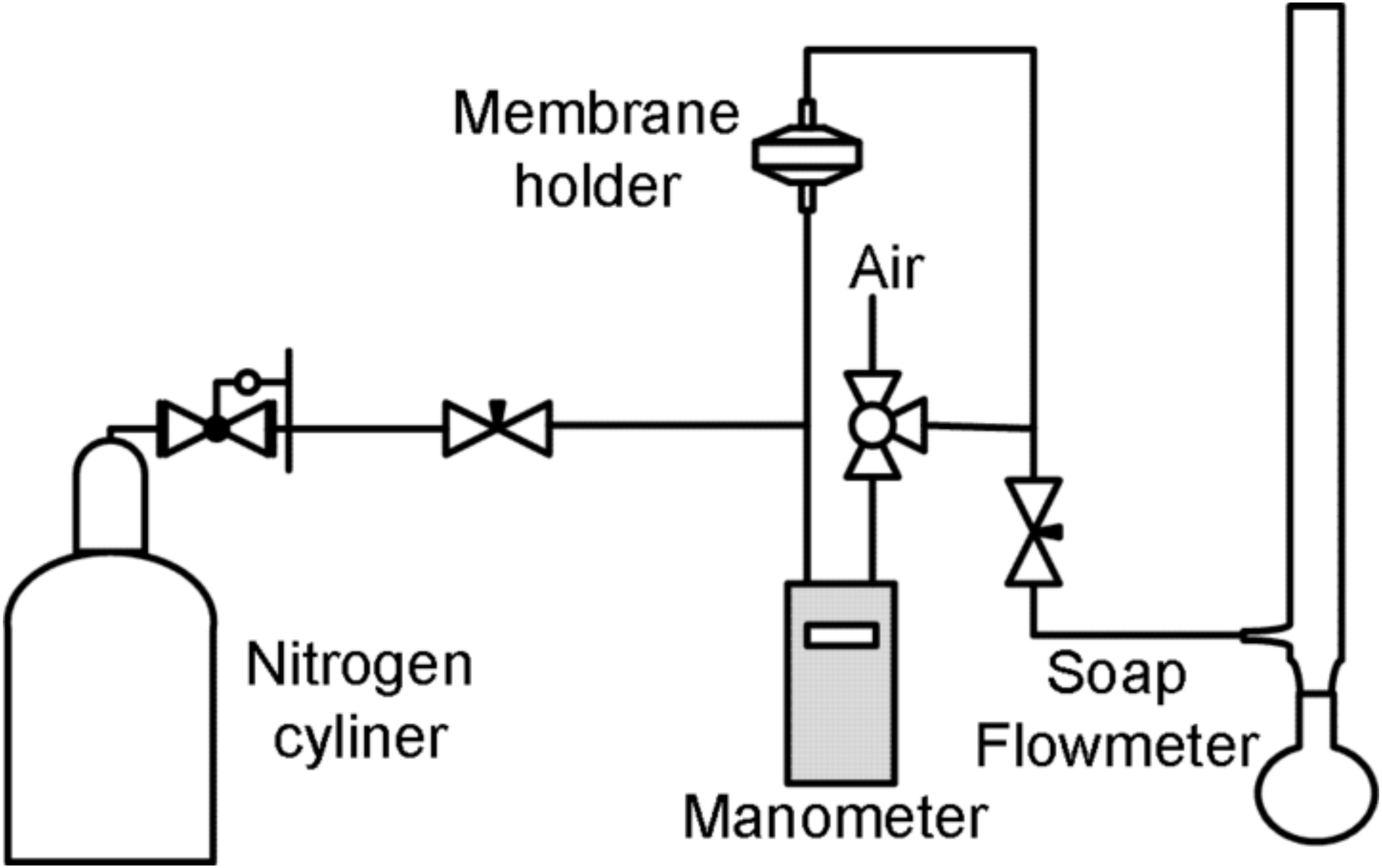
Membrane holder
Air
Nitrogen cyliner
Manometer
Soap Flowmeter

Figure
Click here to download high resolution image

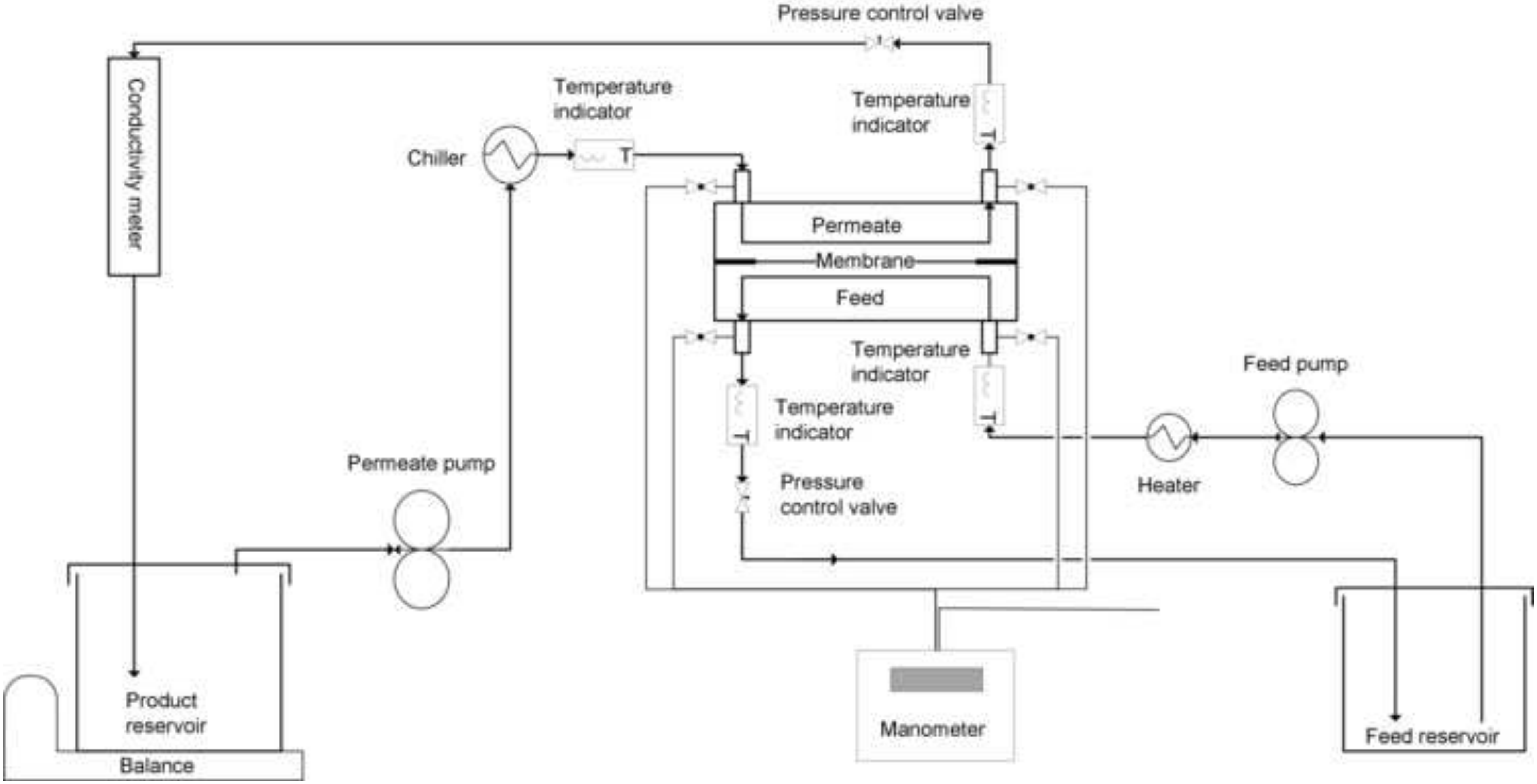
Pressure control valve
Conductivity meter
Temperature indicator
Temperature indicator
Chiller
Permeate
Membrane
Feed
Temperature indicator
Temperature indicator
Feed pump
Permeate pump
Pressure control valve
Heater
Product reservoir
Balance
Manometer
Feed reservoir

Figure
Click here to download high resolution image

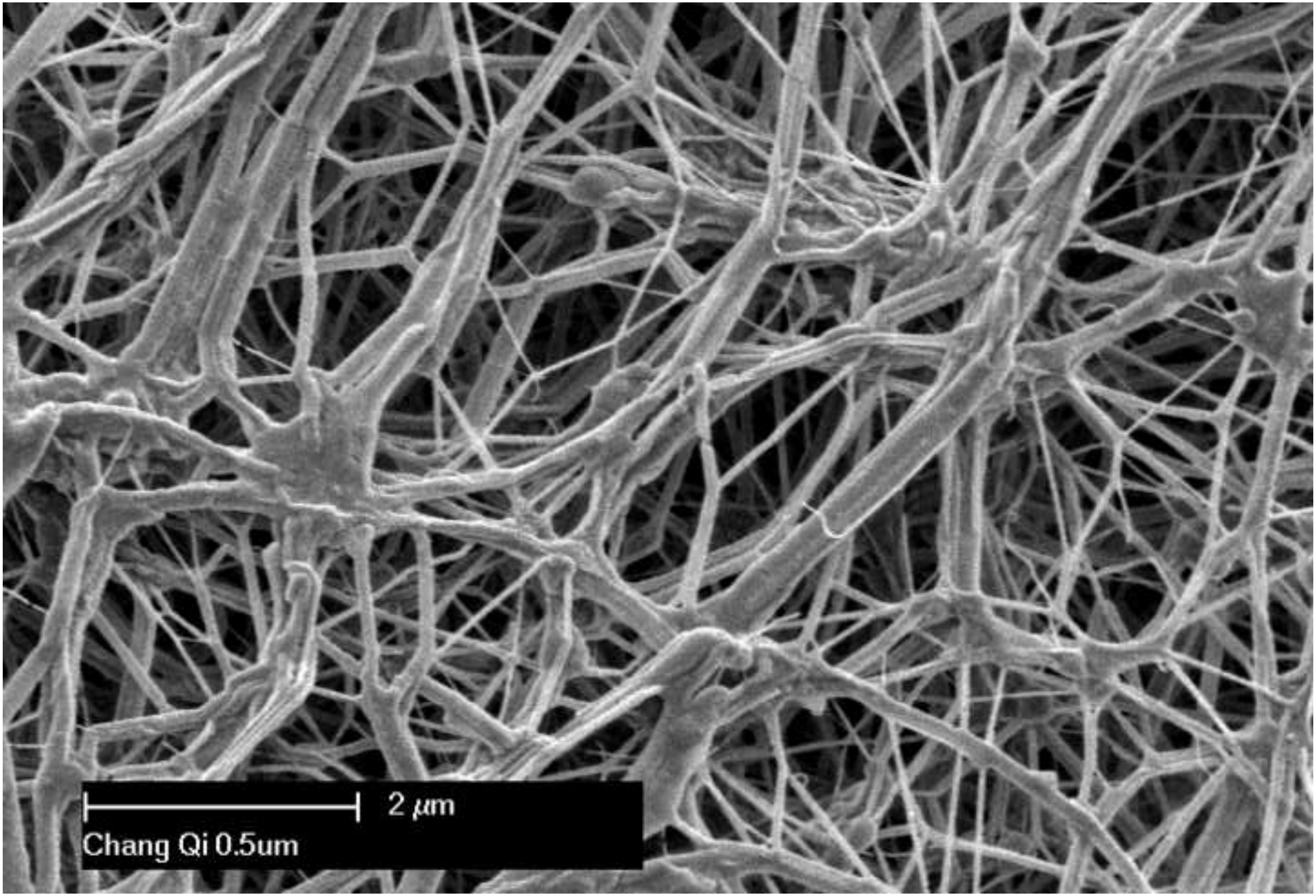
2 μm
Chang Qi 0.5um

Figure
Click here to download high resolution image

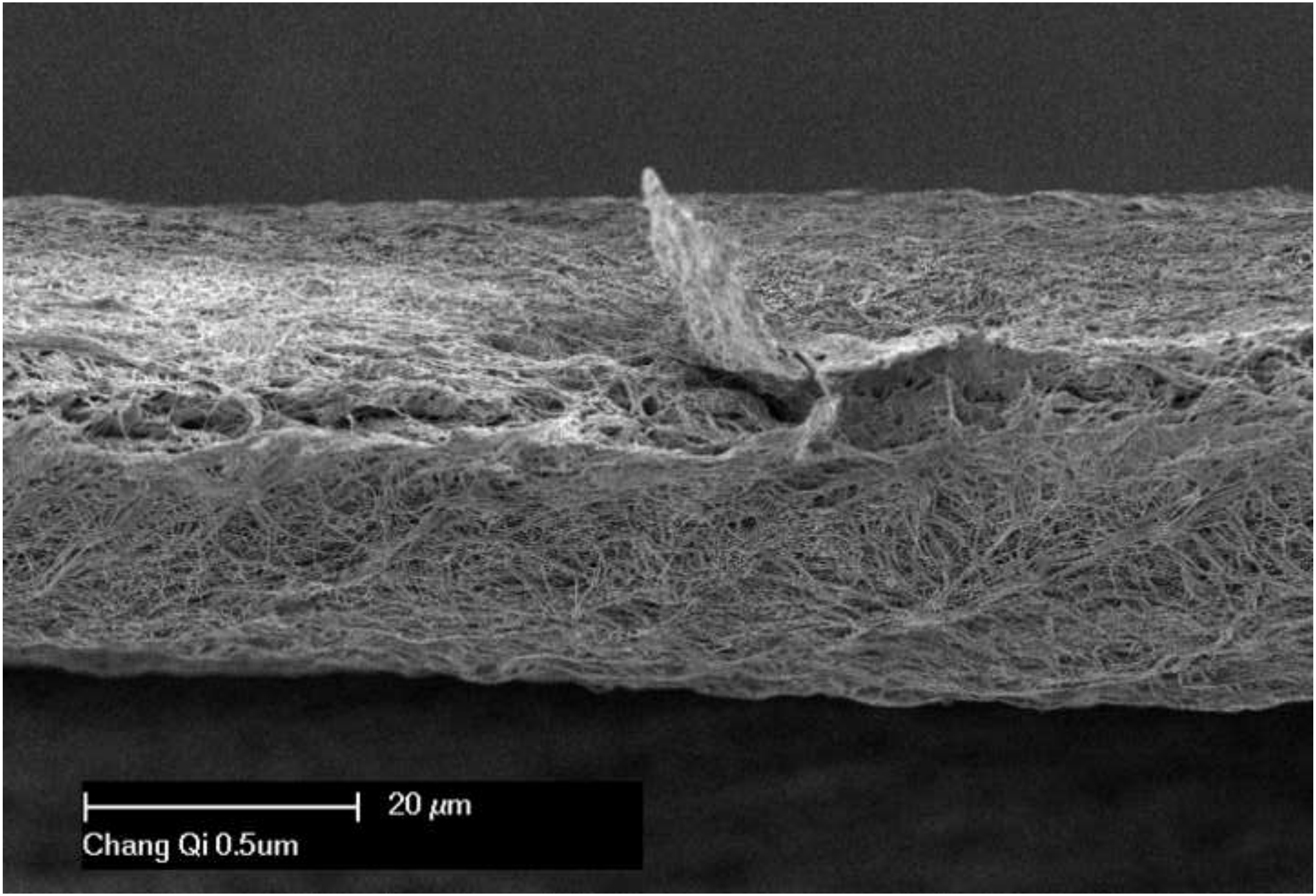
20 µm
Chang Qi 0.5um

Figure
Click here to download high resolution image

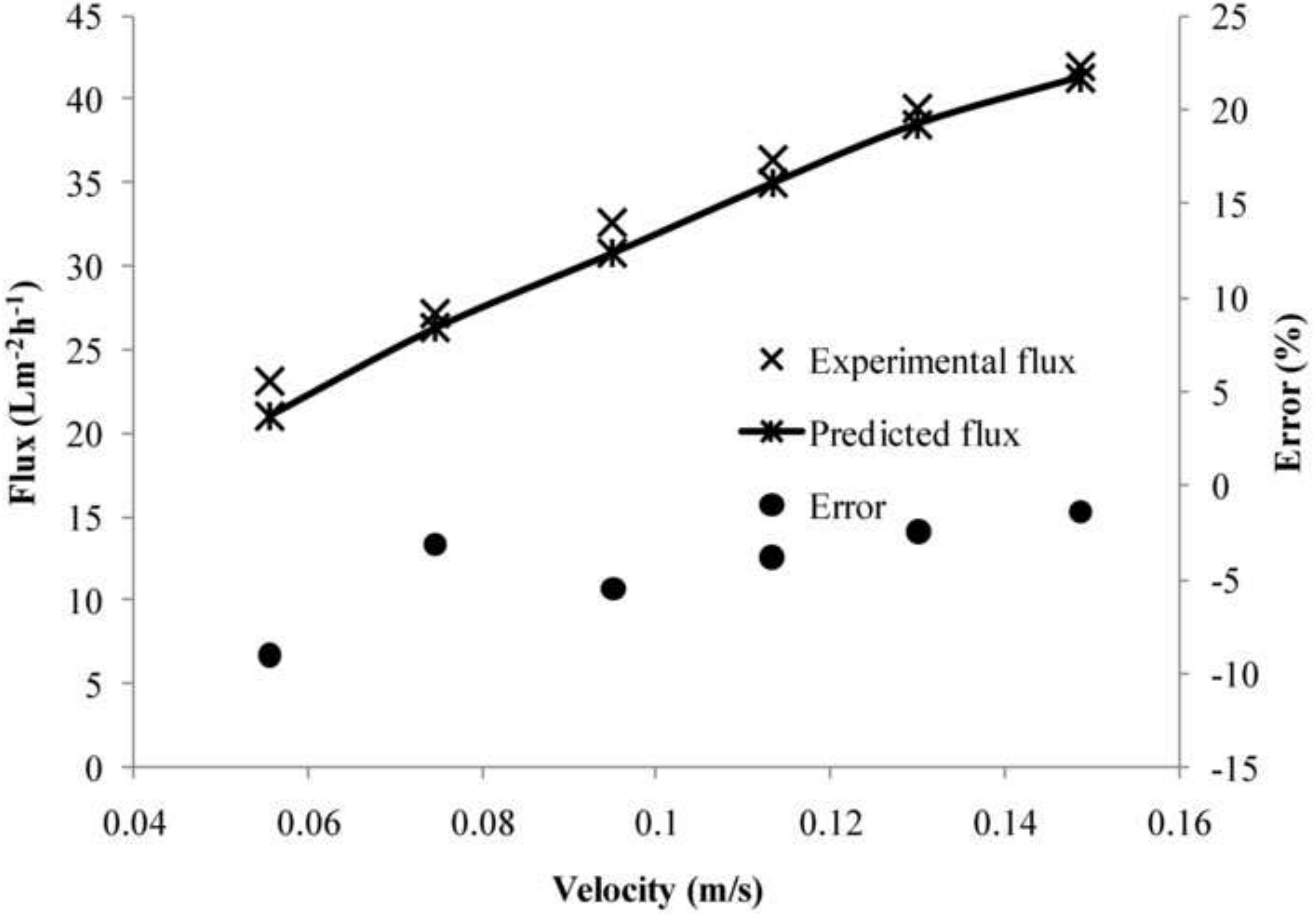

Figure
Click here to download high resolution image

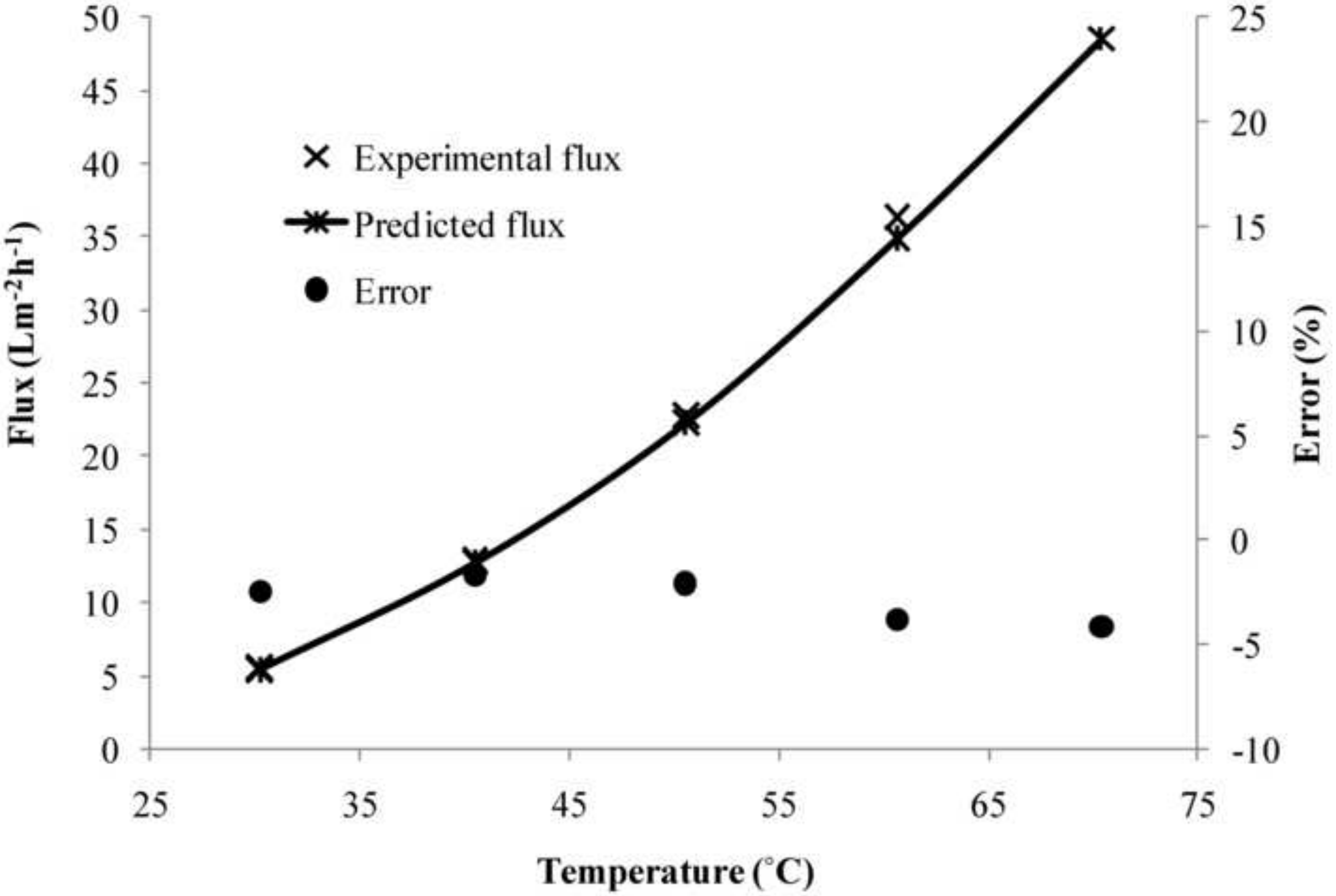

Figure
Click here to download high resolution image

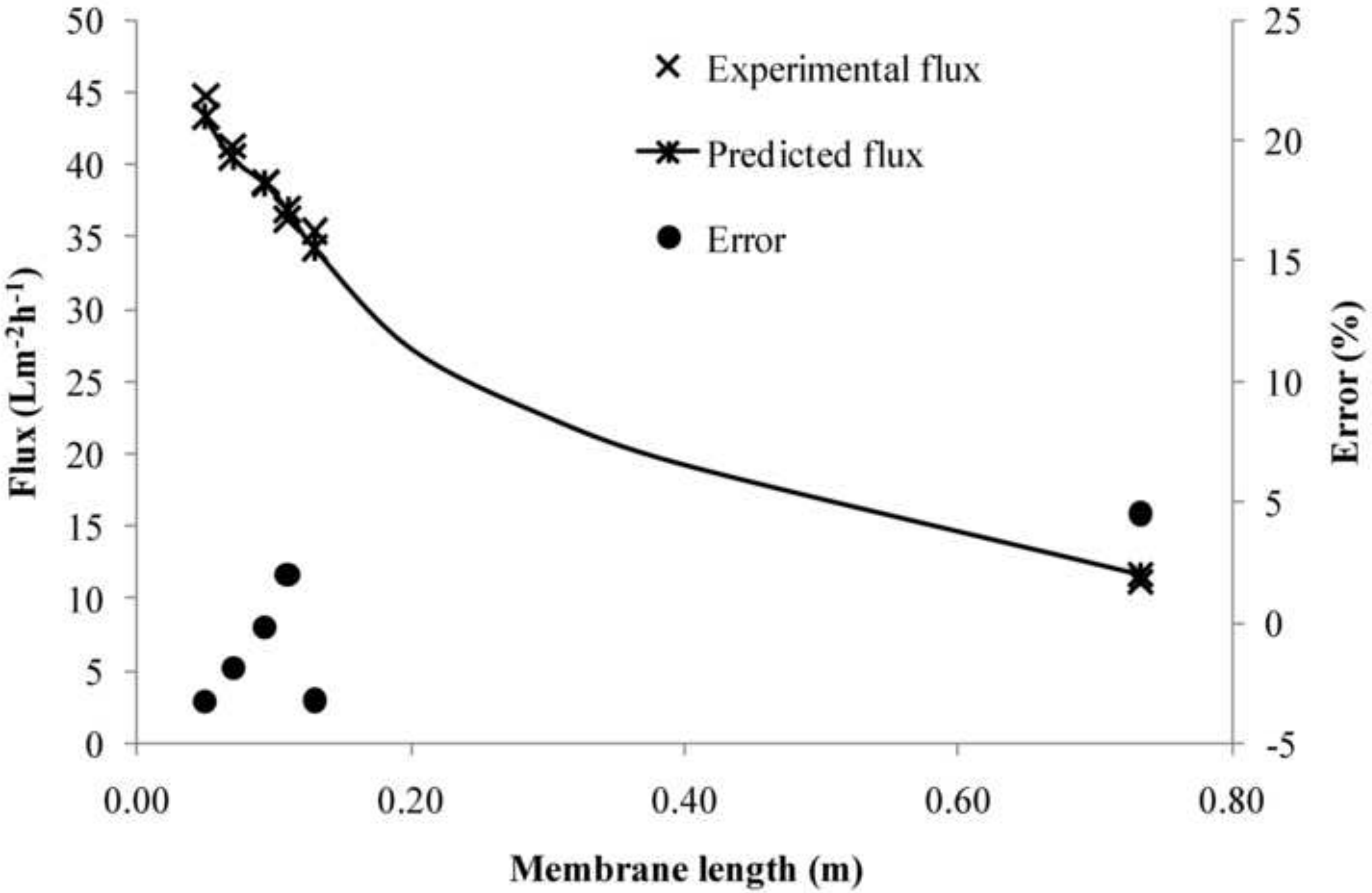

Figure
Click here to download high resolution image

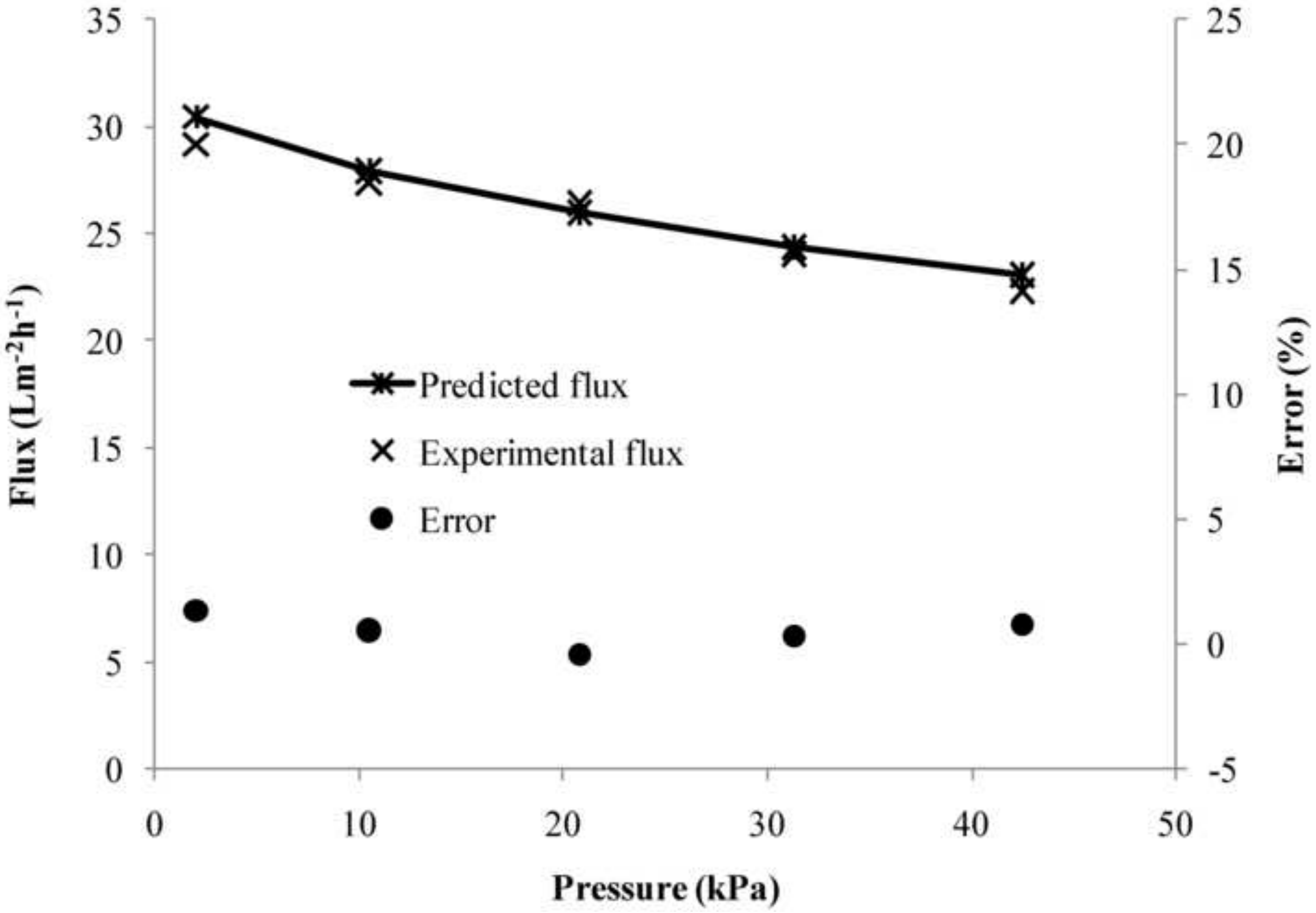

Figure

Click here to download high resolution image

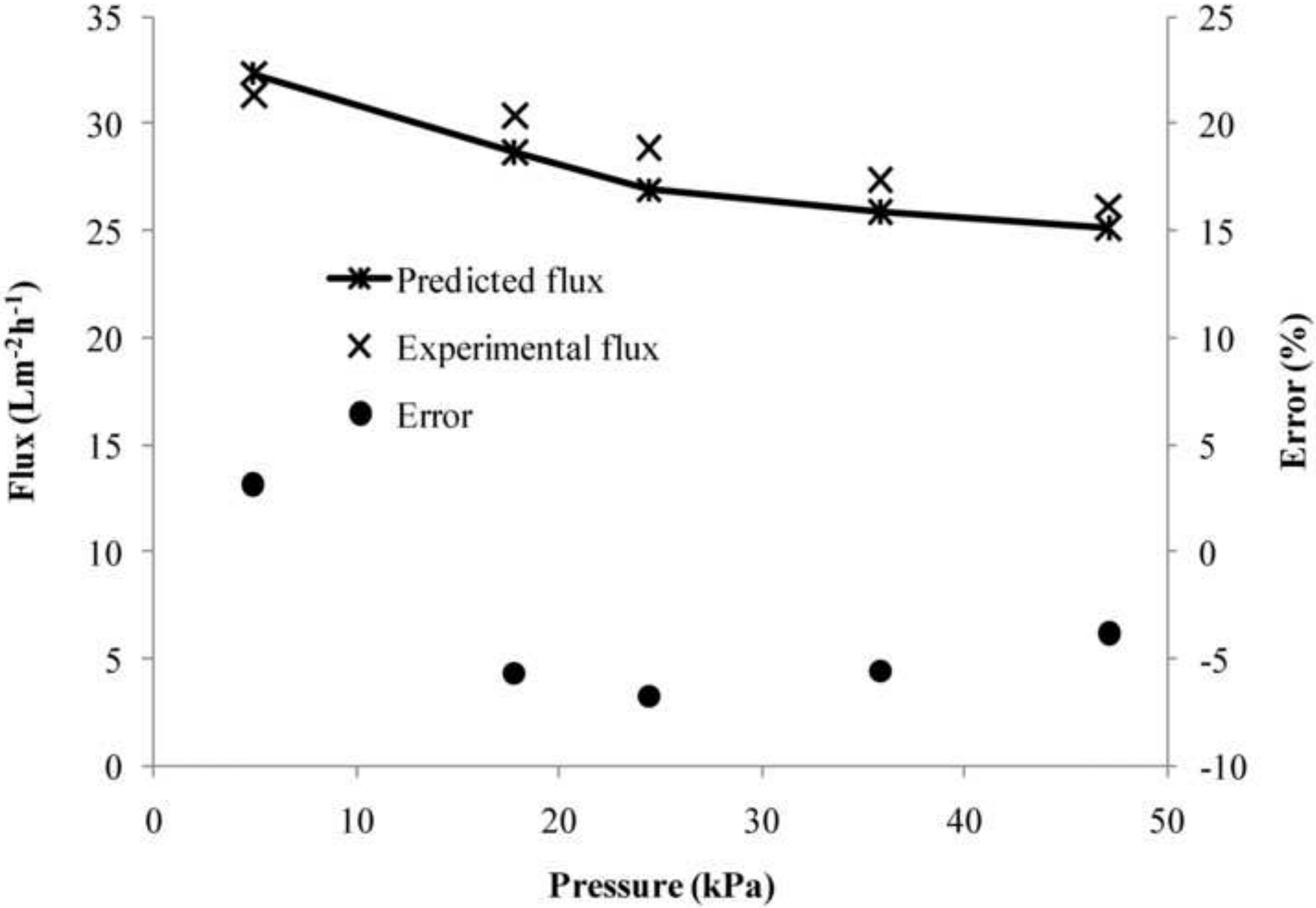

Figure
Click here to download high resolution image

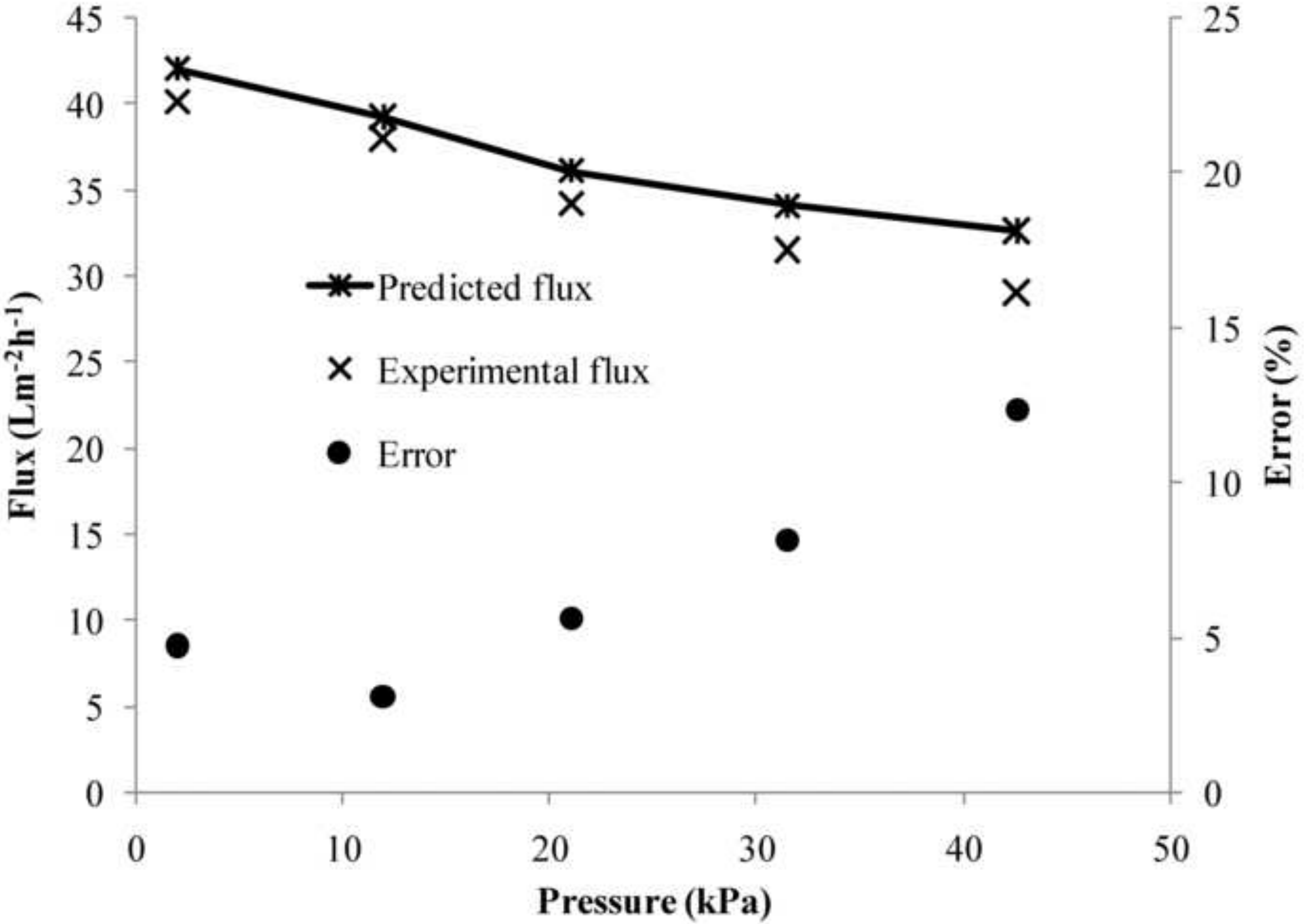

Figure
Click here to download high resolution image

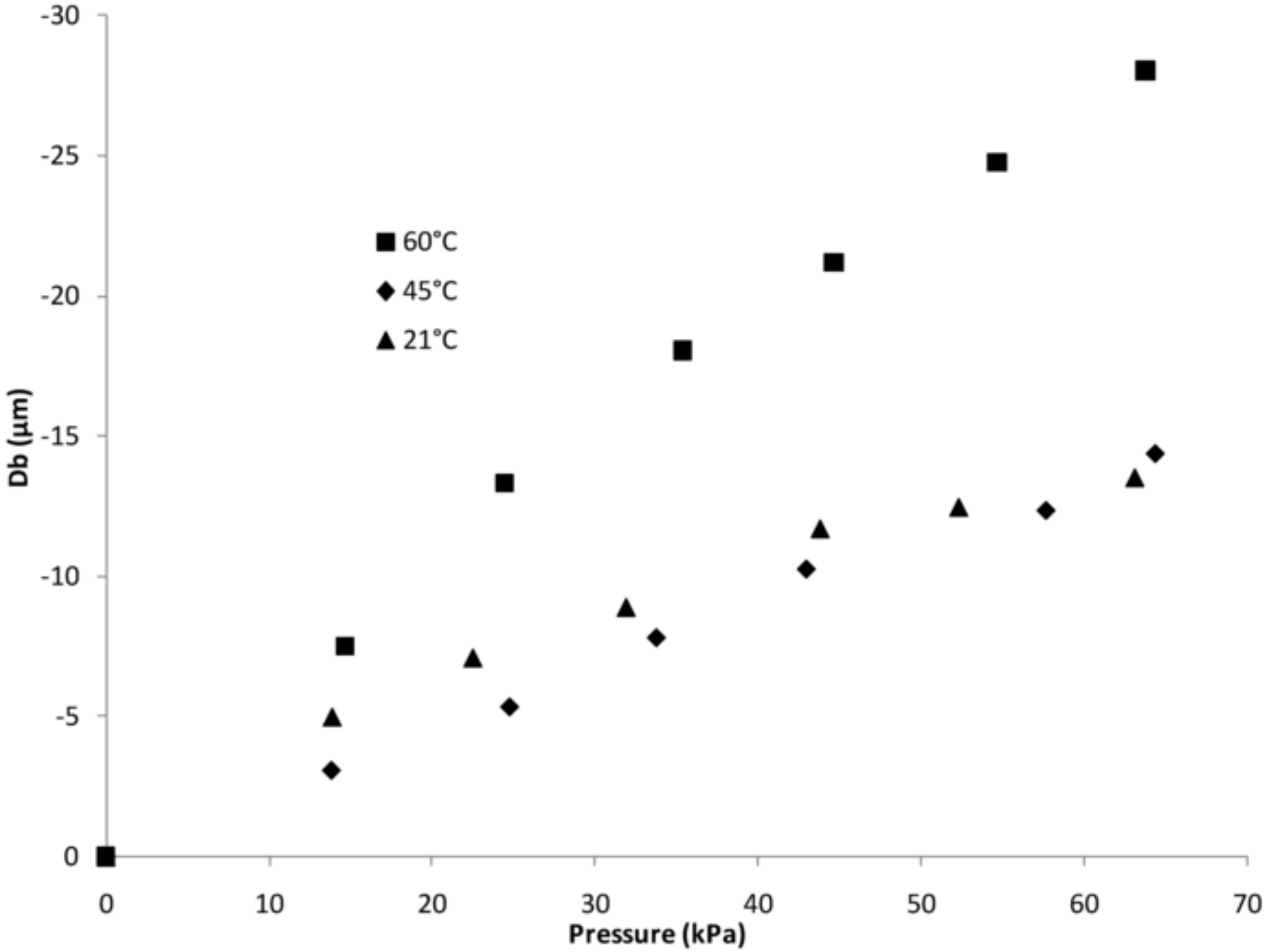

Figure
Click here to download high resolution image

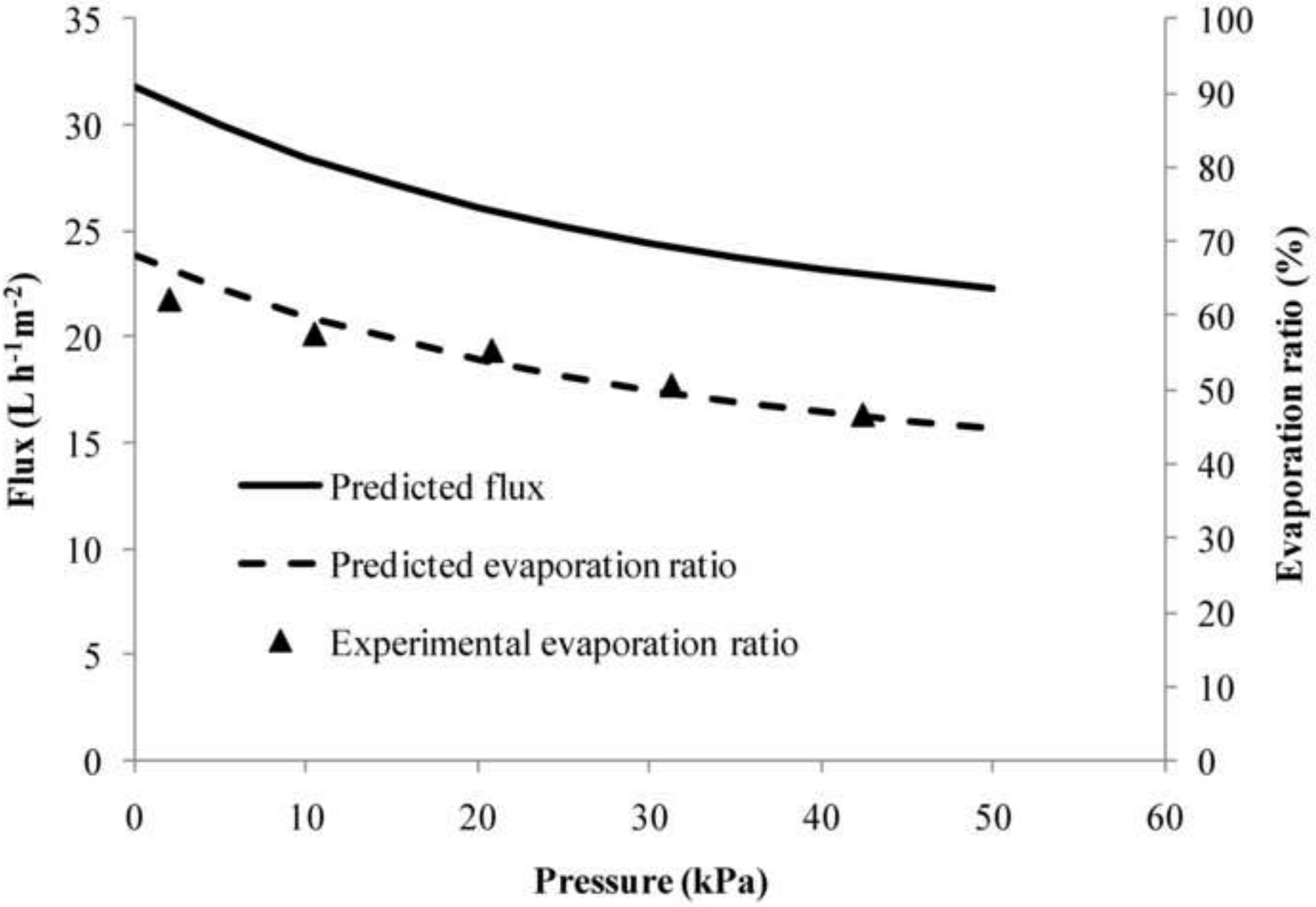

Figure
Click here to download high resolution image

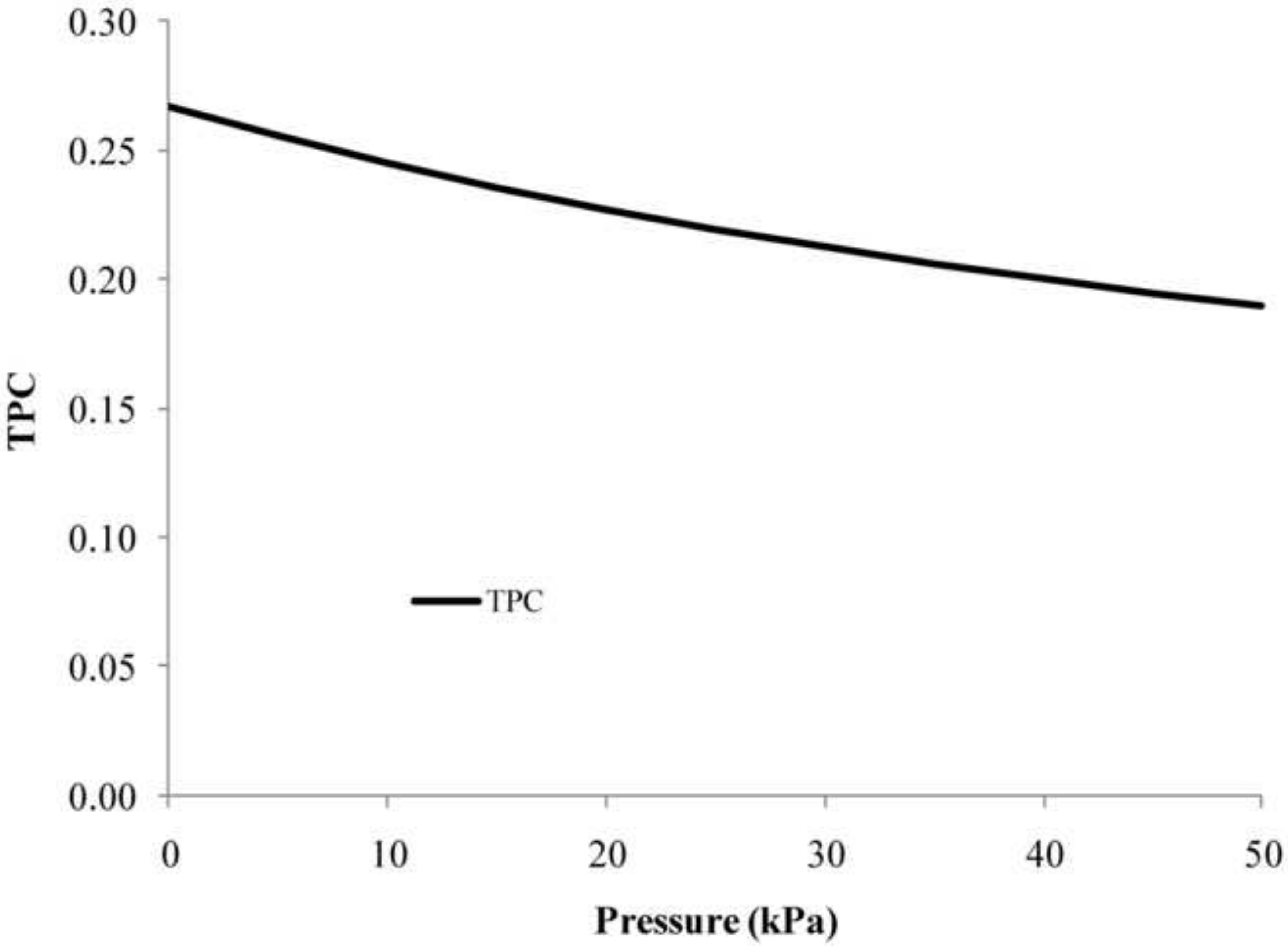

Figure
Click here to download high resolution image

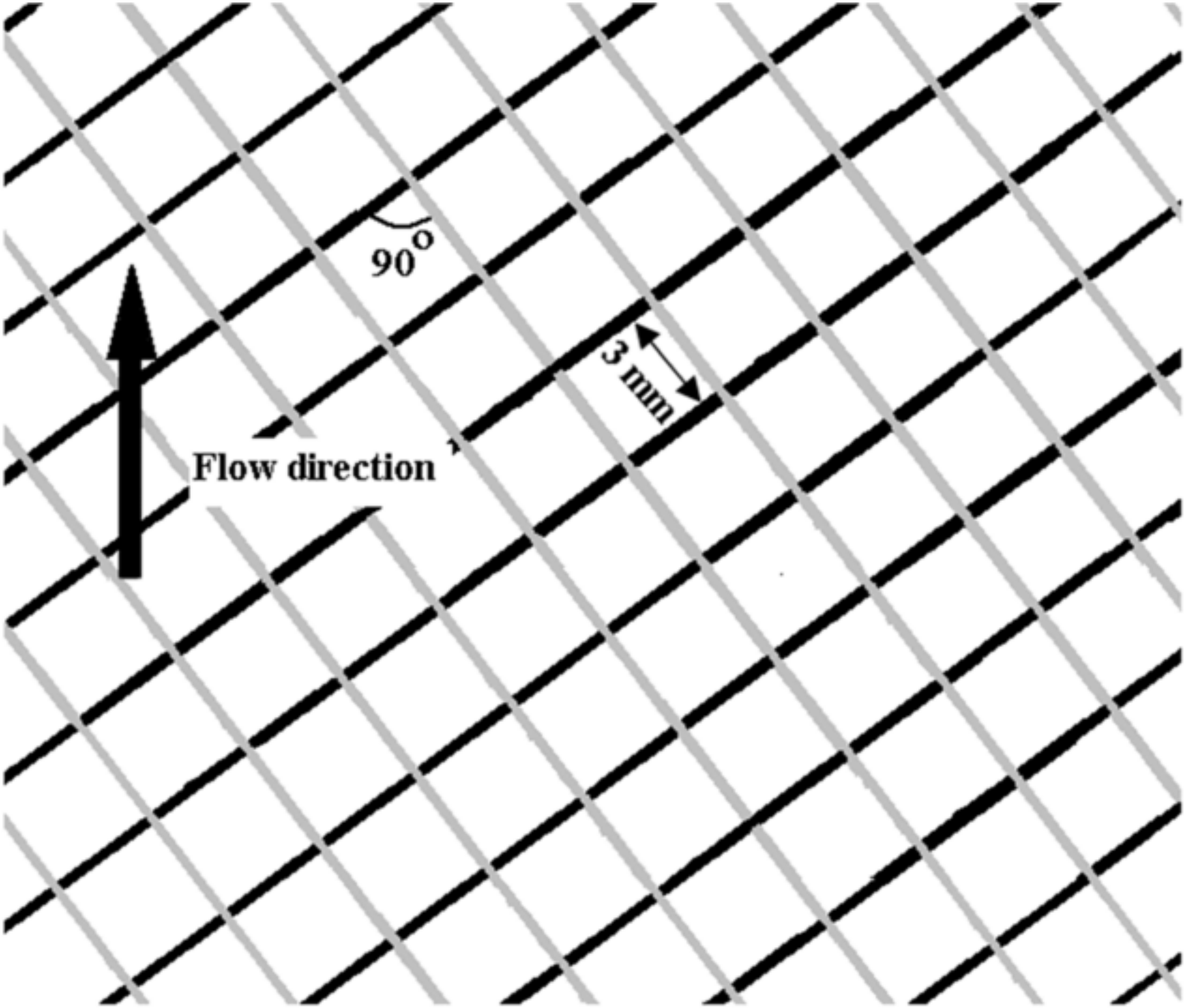
90°
3 mm
Flow direction